PERGAMON

Engineering Fracture Mechanics 69 (2002) 1557–1586

Engineering Fracture Mechanics

www.elsevier.com/locate/engfracmech

Mixed-mode fracture of orthotropic functionally graded materials using finite elements and the modified crack closure method

Jeong-Ho Kim, Glaucio H. Paulino *

Department of Civil and Environmental Engineering, University of Illinois at Urbana-Champaign, Newmark Laboratory, 205 North Mathews Avenue, Urbana, IL 61801, USA

Received 26 September 2001; received in revised form 20 December 2001; accepted 21 December 2001

Abstract

A finite element methodology is developed for fracture analysis of orthotropic functionally graded materials (FGMs) where cracks are arbitrarily oriented with respect to the principal axes of material orthotropy. The graded and orthotropic material properties are smooth functions of spatial coordinates, which are integrated into the element stiffness matrix using the isoparametric concept and special graded finite elements. Stress intensity factors (SIFs) for mode I and mixed-mode two-dimensional problems are evaluated and compared by means of the modified crack closure (MCC) and the displacement correlation technique (DCT) especially tailored for orthotropic FGMs. An accurate technique to evaluate SIFs by means of the MCC is presented using a simple two-step (predictor–corrector) process in which the SIFs are first predicted (e.g. by the DCT) and then corrected by Newton iterations. The effects of boundary conditions, crack tip mesh discretization and material properties on fracture behavior are investigated in detail. Many numerical examples are given to validate the proposed methodology. The accuracy of results is discussed by comparison with available (semi-) analytical or numerical solutions.
© 2002 Elsevier Science Ltd. All rights reserved.

Keywords: Functionally graded material; Stress intensity factor; Modified crack closure; Displacement correlation technique; Finite element method

1. Introduction

Functionally graded materials (FGMs) are special composites in which the volume fraction of constituent materials vary gradually, giving a non-uniform microstructure with continuously graded macroproperties [1]. Functional gradation opens new possibilities for optimizing both material and component structures to achieve high performance and material efficiency. However, at the same time, it also poses challenging mechanics problems including the understanding of damage and fracture behavior of such materials,

* Corresponding author. Tel.: +1-217-333-3817; fax: +1-217-265-8041.
E-mail address: paulino@uiuc.edu (G.H. Paulino).

0013-7944/02/$ - see front matter © 2002 Elsevier Science Ltd. All rights reserved.
PII: S0013-7944(02)00057-7

especially when preferential directions of orthotropy develop due to the material processing technique utilized, as discussed below. Thus the goal of this investigation is to develop a general-purpose finite element framework for fracture of orthotropic FGMs.

With the introduction of the FGM concept, extensive research on various aspects of fracture of *isotropic* FGMs under mechanical [2–4] or thermal [5–11] loads has been conducted. Mode I [12,13] and mixed-mode [14,15] crack problems have been investigated by means of the finite element method (FEM) and the path-independent J_k^*-integral, which includes an extra term for the explicit derivative of strain energy density to account for the material variation. Recently, a simplified method has been proposed in the limit of very small integration domains so that the extra term may be neglected [16]. Multiple cracking [17] and delamination cracking and buckling [18] in isotropic functionally graded ceramic/metal coatings have also been investigated under mechanical and thermal loads using the FEM.

On the other hand, the nature of processing techniques of ceramic–metal FGMs may lead to loss of isotropy. For example, graded materials processed by a *plasma spray* technique generally have a lamellar structure [19]. Flattened splats and relatively weak splat boundaries create an oriented material with higher stiffness and weak cleavage planes parallel to the boundary. Furthermore, graded materials processed by the *electron beam physical vapor deposition* technique could have a columnar structure [20], which result in a higher stiffness in the thickness direction and weak fracture planes perpendicular to the boundary. Thus, such materials would not be isotropic, but orthotropic with material directions that can be considered perpendicular to each other as an initial approximation. Gu and Asaro [21] performed theoretical studies in a four point bending specimen consisting of orthotropic FGMs with varying Poisson's ratio. Ozturk and Erdogan [22,23] used integral equations to investigate Mode I and mixed-mode crack problems in an infinite non-homogeneous orthotropic medium with a crack aligned with one of the material directions considering constant Poisson's ratio. One of the goals of this study is to compare the numerical results (FEM) for stress intensity factors (SIFs) in FGMs with the semi-analytical solutions by Ozturk and Erdogan [22,23].

This paper presents numerical techniques to evaluate SIFs in orthotropic FGMs by means of the FEM. To this end, the modified crack closure (MCC) and the displacement correlation technique (DCT) are specifically tailored for orthotropic FGMs. A general-purpose implementation is presented which is able to handle multiple, interacting, arbitrarily shaped and oriented cracks. The remainder of this paper is organized as follows. Section 2 reviews crack tip fields in orthotropic FGMs. Section 3 presents the DCT, and Section 4 addresses the MCC. Section 5 discusses some aspects of the FEM implementation. In order to assess and validate the above development, Section 6 presents several numerical results which are compared to available numerical and/or semi-analytical solutions. Finally, Section 7 concludes the present investigation.

2. Crack tip fields in orthotropic functionally graded materials

The most general anisotropic form of linear elastic stress–strain relations is given by

$$\varepsilon_{ij} = S_{ijkl}\sigma_{kl} \ (i,j,k,l = 1,2,3), \tag{1}$$

where σ_{ij} is the linear stress tensor, ε_{ij} is the linear strain tensor, and S_{ijkl} is the fourth-order compliance tensor. The compliance tensor has 81 independent components, but, because of the symmetry of σ_{ij} and ε_{ij}, the number of independent components reduces to 36. Furthermore, the existence of a strain energy function provides a reduction of the number of independent components to 21 ($S_{ijkl} = S_{klij}$). In order to represent S_{ijkl} in compact form, a contracted notation a_{ij} may be introduced as follows:

$$\varepsilon_i = a_{ij}\sigma_j, \ a_{ij} = a_{ji} \quad (i,j = 1,2,\ldots,6), \tag{2}$$

where the compliance coefficients, a_{ij}, are related to the elastic properties of the material and

$$\varepsilon_1 = \varepsilon_{11},\ \varepsilon_2 = \varepsilon_{22},\ \varepsilon_3 = \varepsilon_{33},\ \varepsilon_4 = 2\varepsilon_{23},\ \varepsilon_5 = 2\varepsilon_{13},\ \varepsilon_6 = 2\varepsilon_{12}$$
$$\sigma_1 = \sigma_{11},\ \sigma_2 = \sigma_{22},\ \sigma_3 = \sigma_{33},\ \sigma_4 = \sigma_{23},\ \sigma_5 = \sigma_{13},\ \sigma_6 = \sigma_{12}. \tag{3}$$

For the special case of plane stress or plane strain problems in transversely isotropic materials (where at each point through the thickness there is a plane of material symmetry parallel to the plane of the problem), Eq. (2) can be reduced to depend upon six independent elastic parameters for plane stress:

$$a_{ij} \quad (i,j = 1,2,6) \tag{4}$$

and a set of corresponding constants for plane strain:

$$b_{ij} = a_{ij} - \frac{a_{i3}a_{j3}}{a_{33}} \quad (i,j = 1,2,6). \tag{5}$$

Fig. 1 shows a crack tip referred to the Cartesian coordinate systems in orthotropic FGMs. Two dimensional anisotropic elasticity problems can be formulated in terms of the analytic functions, $\phi_k(z_k)$, of the complex variable, $z_k = x_k + \mathrm{i}y_k$ $(k = 1,2)$, where

$$x_k = x + \alpha_k y, \quad y_k = \beta_k y \quad (k = 1,2). \tag{6}$$

The parameters α_k and β_k are the real and imaginary parts of $\mu_k = \alpha_k + \mathrm{i}\beta_k$, which can be determined from [24]

$$a_{11}\mu^4 - 2a_{16}\mu^3 + (2a_{12} + a_{66})\mu^2 - 2a_{26}\mu + a_{22} = 0. \tag{7}$$

The roots μ_k are always complex or purely imaginary in conjugate pairs as μ_1, $\bar{\mu}_1$, μ_2, $\bar{\mu}_2$, of which μ_1 *and* μ_2 *must be calculated at the location of a crack tip for FGMs*.

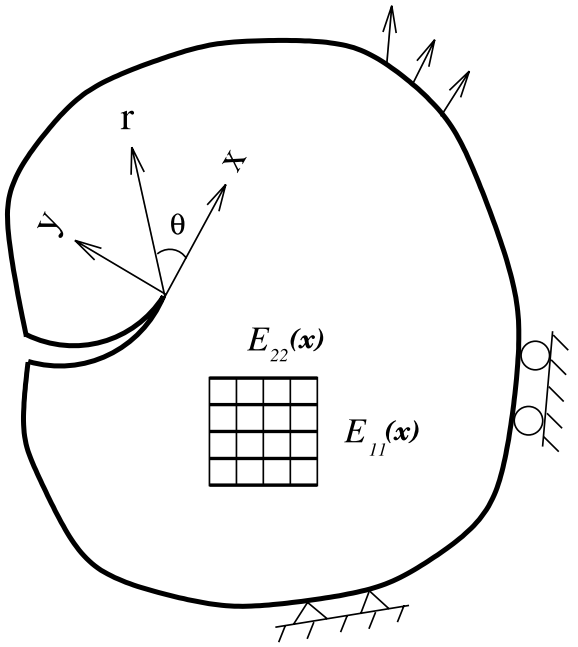

Fig. 1. Coordinate systems at the crack tip in orthotropic FGMs.

For pure mode I, the stresses in the vicinity of the crack tip are

$$\begin{aligned}
\sigma_{11} &= \frac{K_{\mathrm{I}}}{\sqrt{2\pi r}}\mathrm{Re}\left[\frac{\mu_1^{\mathrm{tip}}\mu_2^{\mathrm{tip}}}{\mu_1^{\mathrm{tip}}-\mu_2^{\mathrm{tip}}}\left\{\frac{\mu_2^{\mathrm{tip}}}{\sqrt{\cos\theta+\mu_2^{\mathrm{tip}}\sin\theta}}-\frac{\mu_1^{\mathrm{tip}}}{\sqrt{\cos\theta+\mu_1^{\mathrm{tip}}\sin\theta}}\right\}\right]\\
\sigma_{22} &= \frac{K_{\mathrm{I}}}{\sqrt{2\pi r}}\mathrm{Re}\left[\frac{1}{\mu_1^{\mathrm{tip}}-\mu_2^{\mathrm{tip}}}\left\{\frac{\mu_1^{\mathrm{tip}}}{\sqrt{\cos\theta+\mu_2^{\mathrm{tip}}\sin\theta}}-\frac{\mu_2^{\mathrm{tip}}}{\sqrt{\cos\theta+\mu_1^{\mathrm{tip}}\sin\theta}}\right\}\right]\\
\sigma_{12} &= \frac{K_{\mathrm{I}}}{\sqrt{2\pi r}}\mathrm{Re}\left[\frac{\mu_1^{\mathrm{tip}}\mu_2^{\mathrm{tip}}}{\mu_1^{\mathrm{tip}}-\mu_2^{\mathrm{tip}}}\left\{\frac{1}{\sqrt{\cos\theta+\mu_1^{\mathrm{tip}}\sin\theta}}-\frac{1}{\sqrt{\cos\theta+\mu_2^{\mathrm{tip}}\sin\theta}}\right\}\right]
\end{aligned} \tag{8}$$

and the displacements are

$$\begin{aligned}
u_1 &= K_{\mathrm{I}}\sqrt{\frac{2r}{\pi}}\mathrm{Re}\left[\frac{1}{\mu_1^{\mathrm{tip}}-\mu_2^{\mathrm{tip}}}\left\{\mu_1^{\mathrm{tip}}p_2\sqrt{\cos\theta+\mu_2^{\mathrm{tip}}\sin\theta}-\mu_2^{\mathrm{tip}}p_1\sqrt{\cos\theta+\mu_1^{\mathrm{tip}}\sin\theta}\right\}\right]\\
u_2 &= K_{\mathrm{I}}\sqrt{\frac{2r}{\pi}}\mathrm{Re}\left[\frac{1}{\mu_1^{\mathrm{tip}}-\mu_2^{\mathrm{tip}}}\left\{\mu_1^{\mathrm{tip}}q_2\sqrt{\cos\theta+\mu_2^{\mathrm{tip}}\sin\theta}-\mu_2^{\mathrm{tip}}q_1\sqrt{\cos\theta+\mu_1^{\mathrm{tip}}\sin\theta}\right\}\right].
\end{aligned} \tag{9}$$

Similarly, for pure mode II, the stresses in the vicinity of the crack tip are

$$\begin{aligned}
\sigma_{11} &= \frac{K_{\mathrm{II}}}{\sqrt{2\pi r}}\mathrm{Re}\left[\frac{1}{\mu_1^{\mathrm{tip}}-\mu_2^{\mathrm{tip}}}\left\{\frac{(\mu_2^{\mathrm{tip}})^2}{\sqrt{\cos\theta+\mu_2^{\mathrm{tip}}\sin\theta}}-\frac{(\mu_1^{\mathrm{tip}})^2}{\sqrt{\cos\theta+\mu_1^{\mathrm{tip}}\sin\theta}}\right\}\right]\\
\sigma_{22} &= \frac{K_{\mathrm{II}}}{\sqrt{2\pi r}}\mathrm{Re}\left[\frac{1}{\mu_1^{\mathrm{tip}}-\mu_2^{\mathrm{tip}}}\left\{\frac{1}{\sqrt{\cos\theta+\mu_2^{\mathrm{tip}}\sin\theta}}-\frac{1}{\sqrt{\cos\theta+\mu_1^{\mathrm{tip}}\sin\theta}}\right\}\right]\\
\sigma_{12} &= \frac{K_{\mathrm{II}}}{\sqrt{2\pi r}}\mathrm{Re}\left[\frac{1}{\mu_1^{\mathrm{tip}}-\mu_2^{\mathrm{tip}}}\left\{\frac{\mu_1^{\mathrm{tip}}}{\sqrt{\cos\theta+\mu_1^{\mathrm{tip}}\sin\theta}}-\frac{\mu_2^{\mathrm{tip}}}{\sqrt{\cos\theta+\mu_2^{\mathrm{tip}}\sin\theta}}\right\}\right]
\end{aligned} \tag{10}$$

and the displacements are

$$\begin{aligned}
u_1 &= K_{\mathrm{II}}\sqrt{\frac{2r}{\pi}}\mathrm{Re}\left[\frac{1}{\mu_1^{\mathrm{tip}}-\mu_2^{\mathrm{tip}}}\left\{p_2\sqrt{\cos\theta+\mu_2^{\mathrm{tip}}\sin\theta}-p_1\sqrt{\cos\theta+\mu_1^{\mathrm{tip}}\sin\theta}\right\}\right]\\
u_2 &= K_{\mathrm{II}}\sqrt{\frac{2r}{\pi}}\mathrm{Re}\left[\frac{1}{\mu_1^{\mathrm{tip}}-\mu_2^{\mathrm{tip}}}\left\{q_2\sqrt{\cos\theta+\mu_2^{\mathrm{tip}}\sin\theta}-q_1\sqrt{\cos\theta+\mu_1^{\mathrm{tip}}\sin\theta}\right\}\right].
\end{aligned} \tag{11}$$

In the above equations, μ_1^{tip} and μ_2^{tip} denote the crack tip parameters calculated as the roots of Eq. (7), which are taken such that $\beta_k > 0$ ($k = 1, 2$) and p_k and q_k are given by

$$\begin{aligned}
p_k &= a_{11}(\mu_k^{\mathrm{tip}})^2 + a_{12} - a_{16}\mu_k^{\mathrm{tip}}\\
q_k &= a_{12}\mu_k^{\mathrm{tip}} + \frac{a_{22}}{\mu_k^{\mathrm{tip}}} - a_{26}.
\end{aligned} \tag{12}$$

Moreover, K_{I} and K_{II} denote the mode I and mode II SIFs, respectively.

3. Displacement correlation technique for orthotropic functionally graded materials

The DCT is one of the simplest methods to evaluate SIFs. It consists of correlating numerical results for displacement at specific locations on the crack with available analytical solutions. For quarter point singular elements, the crack opening displacement (COD) and crack sliding displacement (CSD) at $x = -r$ are given by [25]

$$\mathrm{COD}(-r) = (4u_{2,i-1} - u_{2,i-2})\sqrt{\frac{r}{\Delta a}}, \tag{13}$$

$$\mathrm{CSD}(-r) = (4u_{1,i-1} - u_{1,i-2})\sqrt{\frac{r}{\Delta a}}, \tag{14}$$

respectively, where $u_{1,i-1}$, $u_{1,i-2}$, $u_{2,i-1}$, and $u_{2,i-2}$ are the relative displacements with respect to the crack tip in the x_i $(i = 1, 2)$ direction at locations $(i-1)$ and $(i-2)$, r is the distance from the crack tip along the local x_1 direction, and Δa is the characteristic length of the crack tip elements (see Fig. 2).

For $\theta = 180°$, by combination of the two modes, Eqs. (9) and (11) reduce to

$$u_1 = K_{\mathrm{I}}\sqrt{\frac{2r}{\pi}}\mathrm{Re}\left[\frac{i}{\mu_1^{\mathrm{tip}} - \mu_2^{\mathrm{tip}}}(\mu_1^{\mathrm{tip}} q_2 - \mu_2^{\mathrm{tip}} q_1)\right] + K_{\mathrm{II}}\sqrt{\frac{2r}{\pi}}\mathrm{Re}\left[\frac{i}{\mu_1^{\mathrm{tip}} - \mu_2^{\mathrm{tip}}}(q_2 - q_1)\right], \tag{15}$$

$$u_2 = K_{\mathrm{I}}\sqrt{\frac{2r}{\pi}}\mathrm{Re}\left[\frac{i}{\mu_1^{\mathrm{tip}} - \mu_2^{\mathrm{tip}}}(\mu_1^{\mathrm{tip}} p_2 - \mu_2^{\mathrm{tip}} p_1)\right] + K_{\mathrm{II}}\sqrt{\frac{2r}{\pi}}\mathrm{Re}\left[\frac{i}{\mu_1^{\mathrm{tip}} - \mu_2^{\mathrm{tip}}}(p_2 - p_1)\right]. \tag{16}$$

Equating Eq. (13) with Eq. (16), and Eq. (14) with Eq. (15), one obtains

$$K_{\mathrm{I}} = \frac{1}{4}\sqrt{\frac{2\pi}{\Delta a}}\frac{D(4u_{1,i-1} - u_{1,i-2}) - B(4u_{2,i-1} - u_{2,i-2})}{AD - BC}, \tag{17}$$

$$K_{\mathrm{II}} = \frac{1}{4}\sqrt{\frac{2\pi}{\Delta a}}\frac{A(4u_{2,i-1} - u_{2,i-2}) - C(4u_{1,i-1} - u_{1,i-2})}{AD - BC}, \tag{18}$$

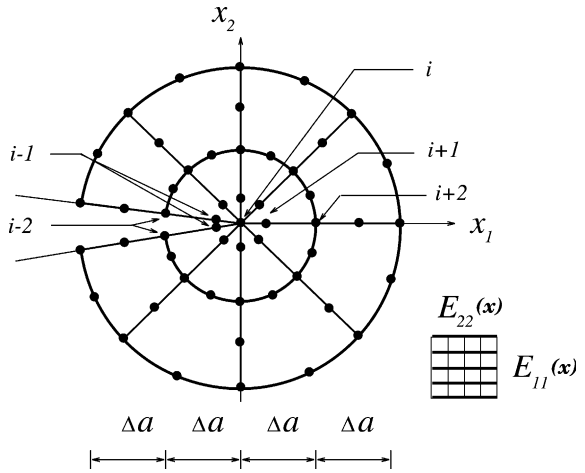

Fig. 2. Crack tip rosette of singular quarter-point (first ring) and regular (second ring) finite elements.

where

$$
\begin{aligned}
A &= \mathrm{Re}\left[\frac{i}{\mu_1^{\mathrm{tip}}-\mu_2^{\mathrm{tip}}}(\mu_1 p_2-\mu_2 p_1)\right]\\
B &= \mathrm{Re}\left[\frac{i}{\mu_1^{\mathrm{tip}}-\mu_2^{\mathrm{tip}}}(p_2-p_1)\right]\\
C &= \mathrm{Re}\left[\frac{i}{\mu_1^{\mathrm{tip}}-\mu_2^{\mathrm{tip}}}(\mu_1 q_2-\mu_2 q_1)\right]\\
D &= \mathrm{Re}\left[\frac{i}{\mu_1^{\mathrm{tip}}-\mu_2^{\mathrm{tip}}}(q_2-q_1)\right],
\end{aligned}
\tag{19}
$$

in which all the material parameters and related coefficients must be considered at the crack tip location for FGMs.

4. Modified crack closure integral for orthotropic functionally graded materials

The MCC integral method is based on Irwin's virtual crack closure approach [26], which uses the stresses ahead of the crack tip and the displacements behind the crack tip. Rybicki and Kanninen [27] used this method to obtain a formula for strain energy release rate with four-node quadrilateral non-singular elements, and Raju [28] extended the method to a set of quarter-point singular elements and provided a modified formulation for the case of crack faces loaded with uniform pressure.

Because no assumption of isotropy or homogeneity around the crack is made, the method is ideally suited for orthotropic FGMs. The energy release rate is estimated only in terms of the work done by the stresses (or equivalent nodal forces) over the displacements behind the crack tip produced by a virtual crack extension.

The expression for $\mathscr{G}_{\mathrm{I}}$ (strain energy release rate for mode I) and $\mathscr{G}_{\mathrm{II}}$ (strain energy release rate for mode II) may be obtained according to Irwin as

$$
\mathscr{G}_{\mathrm{I}} = \lim_{\delta a\to 0}\frac{2}{\delta a}\int_{x_1=0}^{x_1=\delta a}\tfrac{1}{2}\sigma_{22}(r=x_1,\theta=0,a)\,u_2(r=\delta a-x_1,\theta=\pi,a+\delta a)\,\mathrm{d}x_1, \tag{20}
$$

$$
\mathscr{G}_{\mathrm{II}} = \lim_{\delta a\to 0}\frac{2}{\delta a}\int_{x_1=0}^{x_1=\delta a}\tfrac{1}{2}\sigma_{12}(r=x_1,\theta=0,a)\,u_1(r=\delta a-x_1,\theta=\pi,a+\delta a)\,\mathrm{d}x_1, \tag{21}
$$

where $\sigma_{12}\equiv\sigma_{xy}$ and $\sigma_{22}\equiv\sigma_{yy}$ are shear and normal stresses ahead of the crack tip, and $u_1\equiv u_x$ and $u_2\equiv u_y$ are the relative displacements with respect to the crack tip coordinates, respectively. Fig. 3 illustrates a self-similar virtual crack extension δa and the distribution of normal stress ahead of the crack tip.

For the *particular* case in which the material is orthotropic with the crack on a plane of material symmetry, the following relationships are obtained [29]:

$$
\begin{aligned}
\mathscr{G}_{\mathrm{I}} &= K_{\mathrm{I}}^2\sqrt{\frac{a_{11}a_{22}}{2}}\left[\sqrt{\frac{a_{22}}{a_{11}}}+\frac{2a_{12}+a_{66}}{2a_{11}}\right]^{1/2}\\
\mathscr{G}_{\mathrm{II}} &= K_{\mathrm{II}}^2\frac{a_{11}}{\sqrt{2}}\left[\sqrt{\frac{a_{22}}{a_{11}}}+\frac{2a_{12}+a_{66}}{2a_{11}}\right]^{1/2},
\end{aligned}
\tag{22}
$$

where K_{I} and K_{II} are uncoupled.

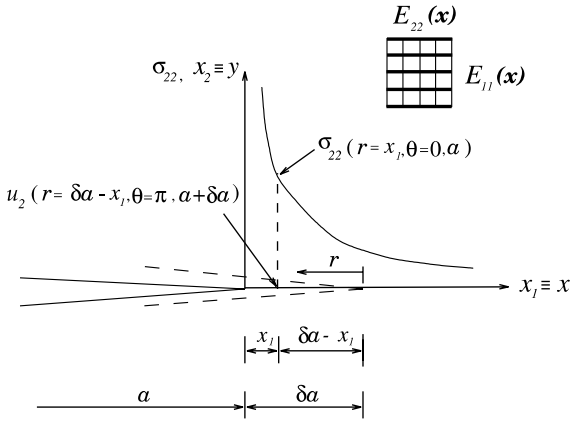

Fig. 3. Self-similiar crack extension and normal stress distribution.

For the *general* case of mixed-mode fracture in orthotropic materials where the crack is arbitrarily oriented with respect to the principal material directions, the SIFs are related to the values of the potential energy release rates through the following expressions [29]:

$$\begin{aligned} \mathscr{G}_{\mathrm{I}} &= -\frac{K_{\mathrm{I}}}{2} a_{22} \mathrm{Im}\left[\frac{K_{\mathrm{I}}(\mu_1^{\mathrm{tip}} + \mu_2^{\mathrm{tip}}) + K_{\mathrm{II}}}{\mu_1^{\mathrm{tip}} \mu_2^{\mathrm{tip}}}\right] \\ \mathscr{G}_{\mathrm{II}} &= \frac{K_{\mathrm{II}}}{2} a_{11} \mathrm{Im}\left[K_{\mathrm{II}}(\mu_1^{\mathrm{tip}} + \mu_2^{\mathrm{tip}}) + K_{\mathrm{I}} \mu_1^{\mathrm{tip}} \mu_2^{\mathrm{tip}}\right]. \end{aligned} \tag{23}$$

For this case, the SIFs are coupled and they may be solved by means of the Newton iteration algorithm summarized below. Define a system of non-linear equations as follows:

$$\begin{aligned} \boldsymbol{F}(\boldsymbol{K}) &= (F_1(\boldsymbol{K}), F_2(\boldsymbol{K})) \\ F_1(\boldsymbol{K}) &= \mathscr{G}_{\mathrm{I}} + \frac{K_{\mathrm{I}}}{2} a_{22} \mathrm{Im}\left[\frac{K_{\mathrm{I}}(\mu_1^{\mathrm{tip}} + \mu_2^{\mathrm{tip}}) + K_{\mathrm{II}}}{\mu_1^{\mathrm{tip}} \mu_2^{\mathrm{tip}}}\right] \\ F_2(\boldsymbol{K}) &= \mathscr{G}_{\mathrm{II}} - \frac{K_{\mathrm{II}}}{2} a_{11} \mathrm{Im}\left[K_{\mathrm{II}}(\mu_1^{\mathrm{tip}} + \mu_2^{\mathrm{tip}}) + K_{\mathrm{I}} \mu_1^{\mathrm{tip}} \mu_2^{\mathrm{tip}}\right], \end{aligned} \tag{24}$$

where $\boldsymbol{F}$ is a vector-valued function of F_1 and F_2, and $\boldsymbol{K}$ is a vector of the unknowns $(K_{\mathrm{I}}, K_{\mathrm{II}})$.

Determination of $(K_{\mathrm{I}}, K_{\mathrm{II}})$ using Newton iteration method:

1. Select $\boldsymbol{K}^{(0)}(K_{\mathrm{I}}, K_{\mathrm{II}})$ and initialize counter $i = 0$.
2. Compute gradient: $\nabla \boldsymbol{F}(\boldsymbol{K})$
3. Perform iteration:

$$\boldsymbol{K}^{(i+1)} = \boldsymbol{K}^{(i)} - \frac{\boldsymbol{F}(\boldsymbol{K}^{(i)})}{\nabla \boldsymbol{F}(\boldsymbol{K}^{(i)})}$$

4. Check convergence: If $|\boldsymbol{F}(\boldsymbol{K}^{(i)})| > \mathrm{TOL}$, then $i \leftarrow i + 1$, and GOTO Step 1.

For the initial values of $\boldsymbol{K}^{(0)}(K_{\mathrm{I}}, K_{\mathrm{II}})$ in Step 1, we may use the SIFs obtained by the DCT because it provides physically reasonable SIF values and accelerates the iterative procedure. *Essentially, this procedure*

is a two-step (predictor–corrector) process in which the SIFs are predicted by the DCT and corrected by Newton iterations for the MCC. However, any judicious choice for the initial values of $\boldsymbol{K}^{(0)}(K_{\mathrm{I}}, K_{\mathrm{II}})$ may also be acceptable, as discussed subsequently in Section 6.

Ramamurthy et al. [30], and Raju [28] have shown that the values of $\mathscr{G}_{\mathrm{I}}$ and $\mathscr{G}_{\mathrm{II}}$ can be written in terms of the equivalent nodal forces $F_2 \equiv F_y$ and $F_1 \equiv F_x$, and the relative nodal displacements u_2 and u_1 when employing quarter-point singular elements around the crack tip (see Fig. 2). For mixed-mode problems, the general expressions for $\mathscr{G}_{\mathrm{I}}$ and $\mathscr{G}_{\mathrm{II}}$ are given by [28]

$$\begin{aligned}
\mathscr{G}_{\mathrm{I}} &= \frac{1}{2\Delta a}[F_{2,i}(t_{11}u_{2,i-2} + t_{12}u_{2,i-1}) + F_{2,i+1}(t_{21}u_{2,i-2} + t_{22}u_{2,i-1}) + F^{\mathrm{T}}_{2,i+2}(t_{31}\bar{u}_{2,i-2} + t_{32}\bar{u}_{2,i-1}) \\
&\quad + F^{\mathrm{B}}_{2,i+2}(t_{31}\hat{u}_{2,i-2} + t_{32}\hat{u}_{2,i-1})] \\
\mathscr{G}_{\mathrm{II}} &= \frac{1}{2\Delta a}[F_{1,i}(t_{11}u_{1,i-2} + t_{12}u_{1,i-1}) + F_{1,i+1}(t_{21}u_{1,i-2} + t_{22}u_{1,i-1}) + F^{\mathrm{T}}_{1,i+2}(t_{31}\bar{u}_{1,i-2} + t_{32}\bar{u}_{1,i-1}) \\
&\quad + F^{\mathrm{B}}_{1,i+2}(t_{31}\hat{u}_{1,i-2} + t_{32}\hat{u}_{1,i-1})],
\end{aligned} \tag{25}$$

where the first subscript in F or u refers to the Cartesian coordinate ($x_1 \equiv x$ or $x_2 \equiv y$), the second subscript refers to the nodal point, the parameters t_{kl} ($k = 1, 2, 3$; $l = 1, 2$) are given by

$$\begin{aligned}
t_{11} &= 14 - \frac{33\pi}{8}, \quad t_{12} = -52 - \frac{33\pi}{2}, \\
t_{21} &= -\frac{7}{2} + \frac{21\pi}{16}, \quad t_{22} = 17 - \frac{21\pi}{4}, \\
t_{31} &= 8 - \frac{21\pi}{8}, \quad t_{32} = -32 + \frac{21\pi}{2}
\end{aligned} \tag{26}$$

and Δa is the characteristic length of singular elements around the crack tip which are six-node quarter-point triangular elements as illustrated in Fig. 2. The superscripts T and B indicate the top and bottom regions of the crack with respect to x_1-axis, and thus F^{T} and F^{B} indicate the forces at the top and bottom surfaces, respectively. The fields $\bar{u}$ and $\hat{u}$ represent the relative displacement of the top and bottom surfaces with respect to the crack tip. For example, at location $(i-1)$ in Fig. 2, $\bar{v}_{y,i-1} = v^{\mathrm{T}}_{y,i-1} - v_{y,i}$ and $\hat{v}_{y,i-1} = v^{\mathrm{B}}_{y,i-1} - v_{y,i}$ where v represent absolute displacements.

Eq. (25) is valid for calculating strain energy release rates for self-similar crack growth when the crack faces are traction free. When the crack faces are pressure loaded, Eq. (25) must be modified. Fig. 4(a) shows a crack tip under a uniform crack face pressure loading, denoted by p, and Fig. 4(b) shows the idea of superposition of computed nodal forces and equivalent nodal forces corresponding to the opposite of the applied pressure when six-node triangular quarter-point (T6qp) singular elements are used. The closure of the crack faces from $a + \Delta a$ to a can be decomposed into two parts. In the first part, the applied pressure is "erased" and, in the second part, the stress free crack faces between $a + \Delta a$ and a are "closed". In the FEM, the first part is equivalent to addition of nodal forces corresponding to the opposite of the applied pressure at all nodes between $a + \Delta a$ and a. For the second part, the general procedure described earlier for the MCC method is used. Thus, the resulting forces at nodes i, $i + 1$, and $i + 2$ are

$$F_{y,i} = F^{\mathrm{c}}_{y,i}, \quad F_{y,i+1} = F^{\mathrm{c}}_{y,i+1} - \frac{2p}{3}\Delta a, \quad F_{y,i+2} = F^{\mathrm{c}}_{y,i+2} - \frac{p}{3}\Delta a. \tag{27}$$

The corrected nodal forces are used to calculate the strain energy release rates.

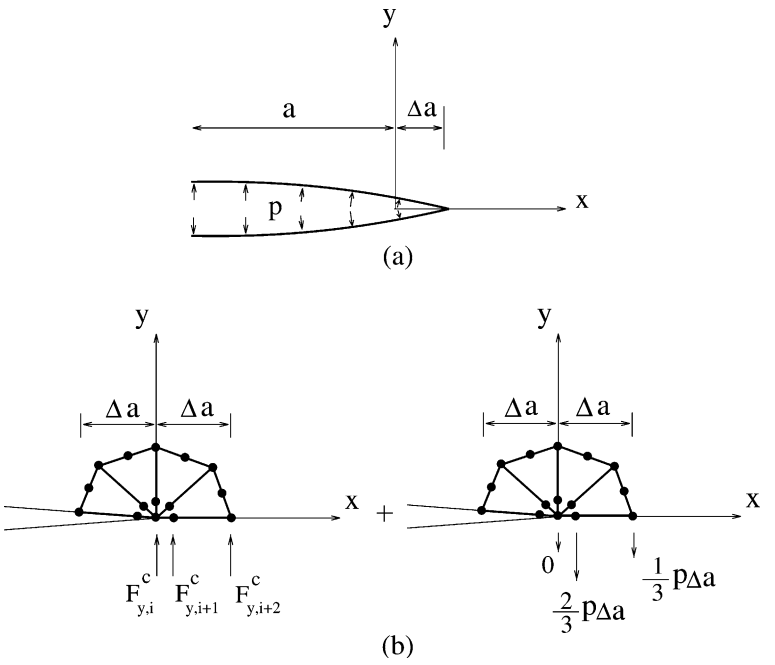

Fig. 4. Modification of nodal forces for uniform crack face pressure loading: (a) crack face pressure loading; (b) superposition of total computed forces and forces needed to account for the pressure loading.

5. Finite element implementation

Graded elements (rather than homogeneous elements) need to be introduced to discretize FGM properties [15,31]. The material properties at Gauss quadrature points are interpolated from the nodal material properties via isoparametric interpolation functions, as illustrated by Fig. 5. The behavior of such graded elements in fracture mechanics of isotropic FGMs has been studied by Paulino and Kim [32]. In order to develop the orthotropic graded elements and perform fracture analyses, the public domain FEM code FRANC2D (FRacture ANalysis Code 2D) [33,34] has been used as the basis for implementing fracture capabilities in FGMs. The source code of FRANC2D is fully accessible and thus it is well-suited for research and for new developments. The code with extended fracture capabilities for FGMs is called I_FRANC2D (Illinois FRacture ANalysis Code 2D). The extensions include special techniques to evaluate

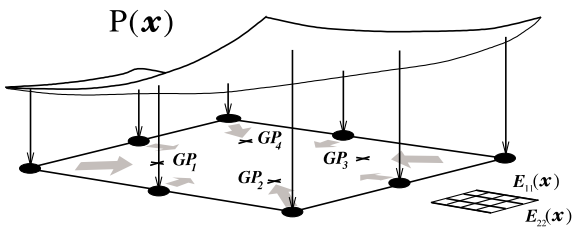

Fig. 5. Generalized isoparametric formulation [15,31] using graded finite elements. The above figure illustrates a graded Q8 element and $P(\boldsymbol{x})$ denotes a generic material property. The Gauss point properties are obtained as $P_{\mathrm{GP}} = \sum N_i P_i$ where $\boldsymbol{N}$ are element shape functions.

SIFs in both isotropic and orthotropic FGMs such as the MCC and DCT, and creation of many sectors and rings around a crack tip. At the crack tip, six-node triangular quarter-point (T6qp) singular elements are used. Eight-node serendipity elements (Q8) are used away from the crack(s), and regular triangular quadratic elements (T6) are used in the transition region between T6qp and Q8 elements. Thus the code allows a careful design of the mesh around the crack tip region, as illustrated by the examples given in the next section.

6. Computational results

This paper examines the elastic stress analysis of orthotropic FGMs and the performance of the MCC and DCT on computing SIFs using the FEM. In order to ascertain the performance of the two methods, the following examples are considered:

(1) Plate with a slanted crack.
(2) Plate with a crack parallel to the material gradation.
(3) Plate with a crack perpendicular to the material gradation.
(4) Two interacting offset cracks.

This set of problems assesses the FEM code and performance of the methods for evaluation of SIFs in orthotropic FGMs. The examples have either numerical (e.g. finite element), semi-analytical (e.g. integral equation) or experimental results available. Thus, the solutions obtained with the I_FRANC2D code are compared with those available results. Moreover, the present solutions can also be verified against other methods for evaluating SIFs in FGMs, e.g. the J_k^*—integral formulation of Kim and Paulino [35].

For the sake of comparison with the semi-analytical solutions by Ozturk and Erdogan [22,23], the following average parameters (originally proposed by Krenk [36]) are used in the second and third examples, as illustrated by Fig. 6(a) and (b), respectively. The independent engineering constants E_{ii}, G_{ij} and v_{ij} $((v_{ij}/E_{ii}) = (v_{ji}/E_{jj}))$ $(i,j = 1,2,3)$ can be replaced by the averaged Young's modulus E, the effective Poisson's ratio v, the stiffness ratio δ^4 and the shear parameter κ_0 [36] defined by

$$E = \sqrt{E_{11}E_{22}}, \quad v = \sqrt{v_{12}v_{21}}, \quad \delta^4 = \frac{E_{11}}{E_{22}} = \frac{v_{12}}{v_{21}}, \quad \kappa_0 = \frac{E}{2G_{12}} - v \tag{28}$$

for generalized plane stress and

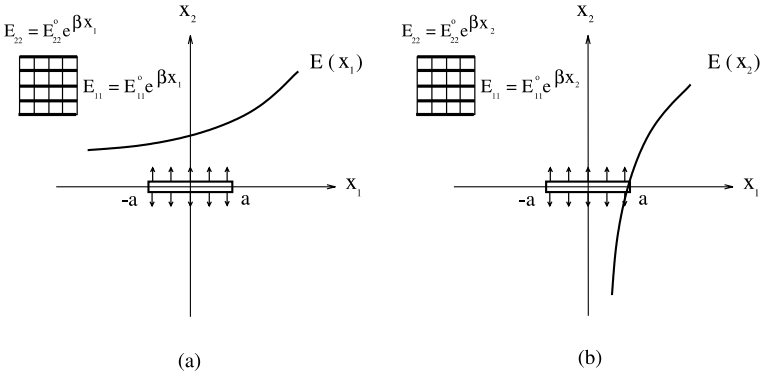

Fig. 6. Geometry and notation for crack problems in an orthotropic non-homogeneous medium: (a) Mode I [22]; (b) mixed-mode [23].

$$E = \sqrt{\frac{E_{11}E_{22}}{(1-\nu_{13}\nu_{31})(1-\nu_{23}\nu_{32})}}, \quad \nu = \sqrt{\frac{(\nu_{12}+\nu_{13}\nu_{32})(\nu_{21}+\nu_{23}\nu_{31})}{(1-\nu_{13}\nu_{31})(1-\nu_{23}\nu_{32})}},$$
$$\delta^4 = \frac{E_{11}(1-\nu_{23}\nu_{32})}{E_{22}(1-\nu_{13}\nu_{31})}, \quad \kappa_0 = \frac{E}{2G_{12}} - \nu \tag{29}$$

for plane strain.

It is worth mentioning that the SIF normalization factor used by Ozturk and Erdogan [22,23] is $k_0 = \sigma\sqrt{a}$ (or $k_0 = \tau\sqrt{a}$) while in this paper $K_0 = \sigma\sqrt{\pi a}$ (or $K_0 = \tau\sqrt{\pi a}$). However, the ratios K_I/K_0 or K_I/k_0 (and K_{II}/K_0 or K_{II}/k_0) are comparable quantities in both pieces of work (i.e. Refs. [22,23] and here) because the $\sqrt{\pi}$ factor cancels out.

6.1. Plate with a slanted crack

Fig. 7(a) shows a slanted crack of length $2a$ located in a finite two-dimensional plate under constant applied tension and Fig. 7(b) shows the complete finite element mesh configuration. Fig. 7(c) shows a detail of the mesh with 4 rings (R4) and 16 sectors (S16) around the crack tips. The mesh has 879 Q8, 430 T6, and 32 T6qp crack tip elements with a total of 1341 elements and 3694 nodes. All the elements are graded and orthotropic [31]. The applied load corresponds to $\sigma_{22}(-10 \leqslant x_1 \leqslant 10, \pm 20) = \pm\sigma = \pm 1.0$ along the top and bottom edges. The displacement boundary condition is prescribed such that $u_1 = u_2 = 0$ for the node in the middle of the left edge and $u_2 = 0$ for the node in the middle of the right edge.

With reference to the example of Fig. 7, the following data were used for the FEM analysis:

$$2a = 2\sqrt{2}, \quad L/W = 2.0,$$
$$E_{11}(x_1) = E_{11}^0 e^{\alpha x_1}, \quad E_{22}(x_1) = E_{22}^0 e^{\beta x_1}, \quad G_{12}(x_1) = G_{12}^0 e^{\gamma x_1},$$
$$E_{11}^0 = 3.5 \times 10^6, \quad E_{22}^0 = 12 \times 10^6, \quad G_{12}^0 = 3 \times 10^6, \quad \nu_{12} = 0.204$$
generalized plane stress, 2×2 Gauss quadrature.

This example is investigated with respect to three different material variations for E_{11}, E_{22} and G_{12}, which are assumed to be exponential functions; while the Poisson's ratio ν_{12} is assumed to be constant. The cases examined are the following:

(1) Homogeneous orthotropic material: $(\alpha, \beta, \gamma) = (0, 0, 0)$.
(2) Orthotropic FGM with proportional material variation: $(\alpha, \beta, \gamma) = (0.2, 0.2, 0.2)$.
(3) Orthotropic FGM with non-proportional material variation: $(\alpha, \beta, \gamma) = (0.5, 0.4, 0.3)$.

In the first case, the solutions obtained are compared with those available in the literature. However, for the other two cases, there are no other solutions available for comparison.

For the homogeneous orthotropic material case with $(\alpha, \beta, \gamma) = (0, 0, 0)$, Table 1 shows the SIFs using the MCC and DCT in comparison with the reference solutions given by Sih et al. [29] (complex variable approach), Atluri et al. [37] (FEM–hybrid displacement model), and Wang et al. [38] (FEM–M integral). The MCC and DCT estimate the SIFs to within 1.3% and 2.2% errors, respectively, with respect to the reference solution by Sih et al. [29].

The orthotropic FGM case with proportional material variation is investigated considering $(\alpha, \beta, \gamma) = (0.2, 0.2, 0.2)$. The importance of the initial values for SIFs (K_I, K_{II}) are elaborated in this example. Fig. 8 shows four possible solutions (four intersection points) for SIFs at the right crack tip, i.e. $(K_I(+a), K_{II}(+a))$:

$$(\mathbf{1.762}, \mathbf{1.439}), \quad (1.3959, -0.9565), \quad (-1.762, -1.439), \quad (-1.3959, 0.9565).$$

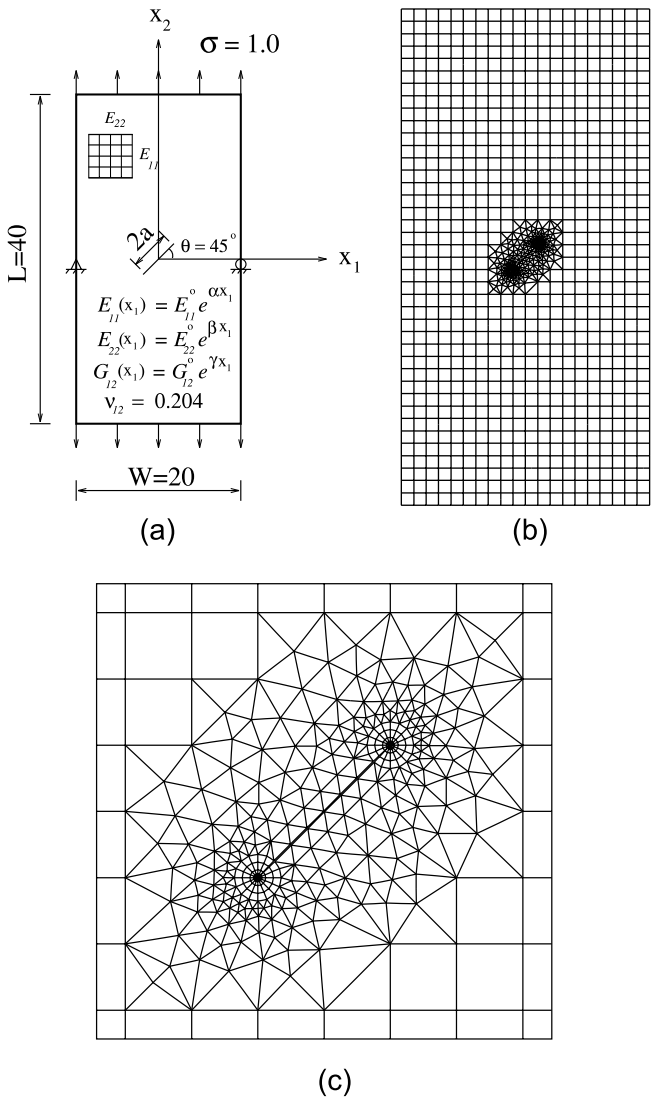

Fig. 7. Plate with a slanted crack: (a) geometry and BCs under remote tension; (b) complete finite element mesh; (c) mesh detail using 4 rings (R4) and 16 sectors (S16) around crack tips.

Initial values for SIFs must be carefully chosen for this problem because there are two sets of admissible solutions for this problem (the first two results above). If we use initial values from the SIFs obtained by the DCT, i.e. $(K_{\mathrm{I}}, K_{\mathrm{II}}) = (1.769, 1.419)$, the final SIFs $(K_{\mathrm{I}}, K_{\mathrm{II}}) = (1.762, 1.439)$ are obtained after two iterations, and are indicated in bold above. However, initial guesses other than the one provided by the DCT may also lead to the correct solution. For instance, we have tried the following initial guesses $(K_{\mathrm{I}}^{(0)}(+a), K_{\mathrm{II}}^{(0)}(+a))$:

$$(1,1), \quad (0.7,0.2), \quad (0.5,0.5) \quad \text{and} \quad (0.2,0.7)$$

and after four, seven, six, and eight iterations, respectively, all of them conducted to the correct solution, i.e. $(K_{\mathrm{I}}(+a), K_{\mathrm{II}}(+a)) = (1.762, 1.439)$. The SIF results for this case are also summarized in Table 1.

Table 1
SIFs in a non-homogeneous orthotropic plate with a slanted crack under uniform remote tension loading (see Fig. 7)

Material	Method	$K_{\mathrm{I}}^{+}(a)$	$K_{\mathrm{II}}^{+}(a)$	$K_{\mathrm{I}}^{-}(a)$	$K_{\mathrm{II}}^{-}(a)$
Homogeneous $(\alpha,\beta,\gamma)=(0,0,0)$	Sih et al. [29]	1.0539	1.0539	1.0539	1.0539
	Atluri et al. [37]	1.0195	1.0795	1.0195	1.0795
	Wang et al. [38]	1.023	1.049	1.023	1.049
	MCC	1.067	1.044	1.067	1.044
	DCT	1.077	1.035	1.077	1.035
FGM (proportional) $(\alpha,\beta,\gamma)=(0.2,0.2,0.2)$	MCC	1.762	1.439	1.403	1.288
	DCT	1.769	1.419	1.419	1.284
FGM (non-proportional) $(\alpha,\beta,\gamma)=(0.5,0.4,0.3)$	MCC	2.384	1.581	1.437	1.225
	DCT	2.387	1.553	1.456	1.229

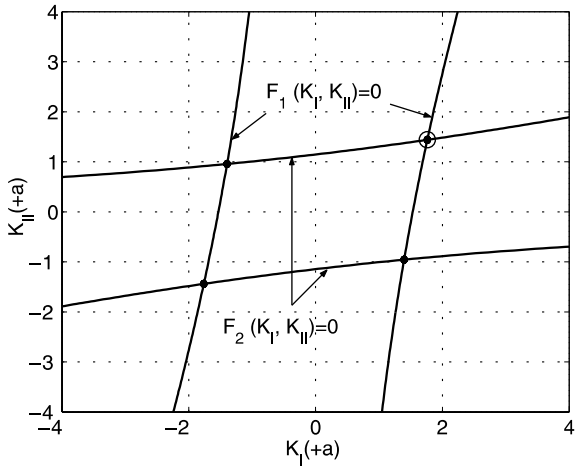

Fig. 8. SIF solutions of non-linear system of equations by Newton's iteration method considering $(\alpha,\beta,\gamma)=(0.2,0.2,0.2)$ (see Fig. 7). The circle around the bullet indicates the converged solution.

The situation depicted by Fig. 8 can change significantly depending on the selection of the material parameters. For instance, if $(\alpha,\beta,\gamma)=(1.0,1.0,1.0)$, the plot in Fig. 9 is obtained, which shows that the roots can be quite close to each other. If we use the SIFs provided by the DCT as initial estimates, i.e. $(K_{\mathrm{I}}(+a),K_{\mathrm{II}}(+a))=(0.7274,0.1553)$, then the final SIFs $(K_{\mathrm{I}}(+a),K_{\mathrm{II}}(+a))=(0.7387,0.1611)$ are obtained after two iterations.

Finally, the orthotropic FGM case with non-proportional material variation is investigated considering $(\alpha,\beta,\gamma)=(0.5,0.4,0.3)$. The SIF results are also summarized in Table 1. Notice that both MCC and DCT provide symmetric SIF responses at the left and right tips for the homogeneous case, while such symmetry is lost for the FGM case (as expected).

6.2. Plate with a crack parallel to material gradation

Ozturk and Erdogan [22] have investigated the Mode I crack problem for an infinite non-homogeneous orthotropic medium as illustrated by Fig. 6(a). Here the infinite medium is approximated by a square plate

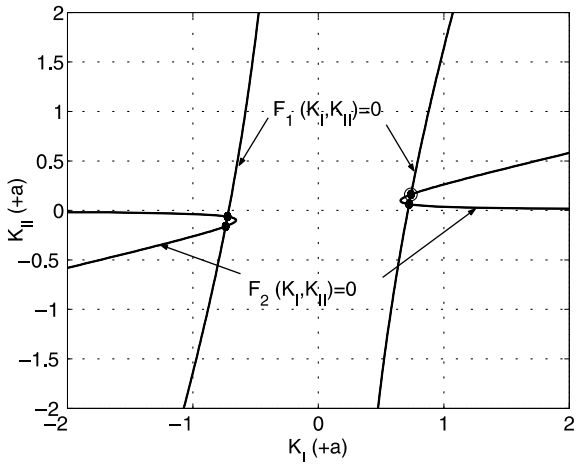

Fig. 9. SIF solutions of non-linear system of equations by Newton's iteration method considering $(\alpha, \beta, \gamma) = (1.0, 1.0, 1.0)$ (see Fig. 7). The circle around the bullet indicates the converged solution.

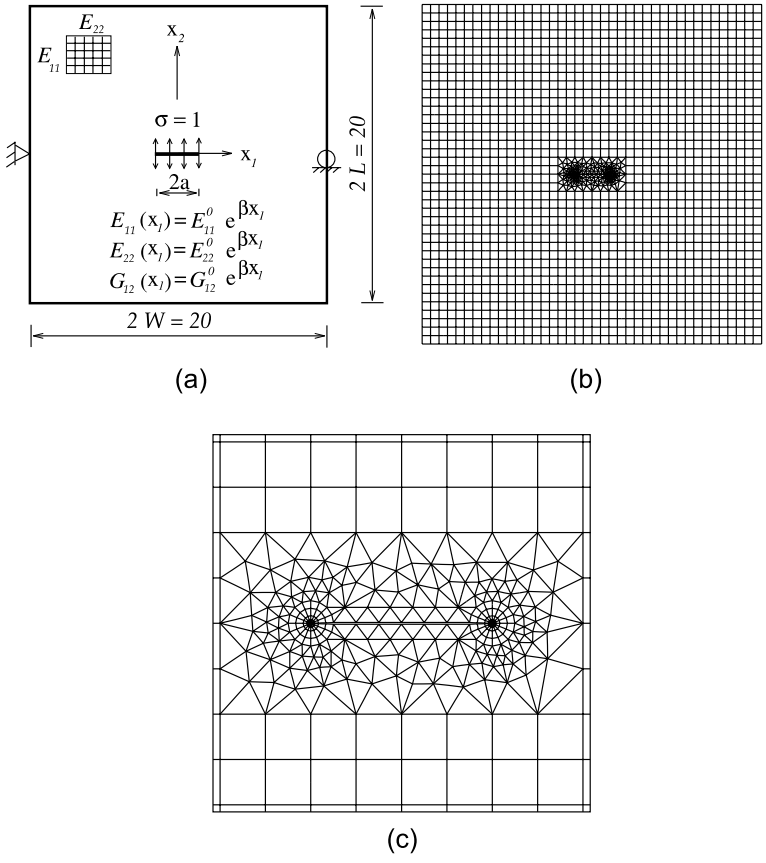

Fig. 10. Plate with a center crack parallel to the material gradation: (a) geometry and BCs under crack face loading; (b) complete finite element mesh; (c) mesh detail using 4 rings (R4) and 16 sectors (S16) around crack tips.

where the ratio of the plate edge length over the crack length is equal to 10. Fig. 10(a) shows a crack of length $2a$ located in a finite two-dimensional plate under uniform crack pressure loading, and Fig. 10(b) shows the corresponding mesh configuration. Notice that the crack is parallel to the material gradation as the average Young's modulus $E \equiv E(x_1) = E^0 e^{\beta x_1}$ where $E^0 = \sqrt{E_{11}^0 E_{22}^0}$. Fig. 10(c) shows a detail with 4 rings (R4) and 16 sectors (S16) around the crack tips. The displacement boundary condition is prescribed such that $u_1 = u_2 = 0$ for the node in the middle of the left edge and $u_2 = 0$ for the node in the middle of the right edge. The applied load corresponds to $\sigma_{22}(-1 \leqslant x_1 \leqslant 1, \pm 0) = \pm\sigma = \pm 1.0$ along the crack faces, as illustrated by Fig. 10(a).

As illustrated by Fig. 10(a), the variations of E_{11}, E_{22}, and G_{12} are assumed to be exponential functions of x_1 and proportional to one another, while the Poisson's ratio v_{12} is constant. The mesh has 1666 Q8, 303 T6, and 32 T6qp singular elements with a total of 2001 elements and 5851 nodes. The following data were used for the FEM analysis:

$$
\begin{aligned}
&a/W = 0.1, \quad L/W = 1.0,\\
&E_{11}(x_1) = E_{11}^0 e^{\beta x_1}, \quad E_{22}(x_1) = E_{22}^0 e^{\beta x_1}, \quad G_{12}(x_1) = G_{12}^0 e^{\beta x_1},\\
&\beta a = (0.0\text{–}1.0), \quad \kappa_0 = (-0.25, 5.0), \quad v = 0.3\\
&\text{generalized plane stress}, \quad 2 \times 2 \text{ Gauss quadrature.}
\end{aligned}
$$

The average modulus indicated above can be rewritten as $E = E^0 e^{(\beta a)(x_1/a)}$, and thus the non-homogeneity parameter β enters the analysis through the dimensionless constant βa. Table 2 reports the normalized SIFs using the MCC and DCT in an orthotropic plate under crack face pressure loading for various βa and for two different values of the shear parameter κ_0, which are compared with the results reported by Ozturk and Erdogan [22]. Both the MCC and the DCT estimate the SIFs within 4% of the results by Ozturk and Erdogan [22]. The influence of κ_0 on K_I (and u_2) appears to be less significant than that of βa. Notice that, in Table 2, the SIFs on the stiffer side of the plate are always greater than those on the less stiff side. Although this result may seem counter intuitive, it can be explained by comparing the displacement profiles of the non-homogeneous medium with those of the homogeneous medium [22]. Fig. 11 plots the crack opening displacements in a non-homogeneous medium with $E(x_1) = E^0 e^{x_1/a}$ and also in homogeneous materials with $E(-a) = E^0 e^{-1.0}$, $E = E^0$, and $E(a) = E^0 e^{1.0}$. When comparing the solution of a non-homogeneous medium with that of a homogeneous medium with the same material properties at the right crack tip $(x_1 = a)$, one can observe that because the crack opening displacement in the non-homogeneous medium is greater than that in the corresponding homogeneous medium $(E(a) = E^0 e^{1.0})$, the SIF (K_I) in the non-homogeneous medium is greater than that in the homogeneous medium. Similarly, for the same material properties at the left crack tip $(x_1 = -a)$, the SIF (K_I) in the non-homogeneous medium is lower than that in the corresponding homogeneous medium $(E(-a) = E^0 e^{-1.0})$. In Fig. 11, the crack opening displacement considering $E = E^0$ serves as a reference curve between those curves for $E = E^0 e^{1.0}$ and $E = E^0 e^{-1.0}$.

6.3. Plate with a crack perpendicular to material gradation

Ozturk and Erdogan [23] have also investigated the mixed-mode crack problem for an infinite non-homogeneous orthotropic medium (see Fig. 6(b)). Similarly to the previous example, the infinite medium is approximated by a square plate where the ratio of the plate edge length over the crack length is equal to 10. The material parameters $E_{11}(\boldsymbol{x})$, $E_{22}(\boldsymbol{x})$ and $G_{12}(\boldsymbol{x})$ are exponentially graded as functions of x_2 and proportional, while the Poisson's ratio v_{12} is constant. The following data were used for the FEM analysis:

Table 2
The normalized SIFs in a non-homogeneous orthotropic plate under uniform crack face loading for mode I problem ($K_0 = \sigma\sqrt{\pi a}$)

Method	βa	$\kappa_0 = -0.25$		$\kappa_0 = 5.0$	
		$K_I^+(a)/K_0$	$K_I^-(a)/K_0$	$K_I^+(a)/K_0$	$K_I^-(a)/K_0$
Ozturk and Erdogan [23]	0.0	1.0	1.0	1.0	1.0
	0.01	1.0025	0.9975	1.0025	0.9975
	0.1	1.0246	0.9747	1.0231	0.9733
	0.25	1.0604	0.9364	1.0531	0.9306
	0.50	1.1177	0.8740	1.0946	0.8594
	0.75	1.1720	0.8154	1.1281	0.7932
	1.00	1.2235	0.7616	1.1556	0.7339
	1.50	1.3184	0.6701	1.1979	0.6367
	2.00	1.4043	0.5979	1.2290	0.5636
MCC S16, $\Delta a = a/24$	0.0	1.005	1.005	1.012	1.012
	0.01	1.007	1.003	1.015	1.009
	0.1	1.034	0.9816	1.041	0.9873
	0.25	1.081	0.9467	1.082	0.9484
	0.50	1.1390	0.8761	1.1255	0.8688
	0.75	1.1819	0.8073	1.1486	0.792
	1.00	1.2293	0.7503	1.1706	0.7278
	1.50	1.3275	0.6572	1.2135	0.6268
	2.00	1.4206	0.5839	1.2496	0.5524
DCT S16, $\Delta a = a/24$	0.0	0.9895	0.9895	1.020	1.020
	0.01	0.9918	0.9873	1.022	1.017
	0.1	1.015	0.9685	1.046	0.9978
	0.25	1.057	0.9372	1.084	0.9613
	0.50	1.107	0.8720	1.120	0.8869
	0.75	1.1419	0.8105	1.1362	0.8141
	1.00	1.1808	0.7577	1.1501	0.7533
	1.50	1.3444	0.6979	1.2017	0.6606
	2.00	1.4307	0.6262	1.2259	0.5884

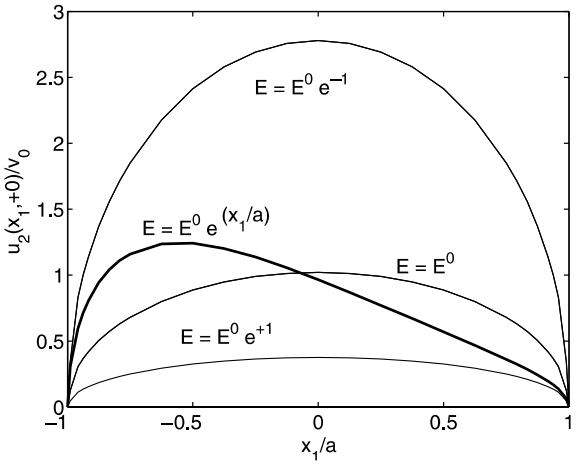

Fig. 11. COD u_2 in a non-homogeneous orthotropic medium under uniform crack face pressure loading where $v_0 = (s_1 + s_2)a\sigma\delta/E^0$ with $s_1 = \sqrt{\kappa_0 + \kappa_1}$, $s_2 = \sqrt{\kappa_0 - \kappa_1}$, $\kappa_1 = \sqrt{\kappa_0^2 - 1}$, $\kappa_0 = 0.5$, $v = 0.3$, and $\beta a = 1.0$. The COD for the crack in the FGM is indicated by a thicker line.

$a/W = 0.1, \quad L/W = 1.0,$

$E_{11}(x_2) = E^0_{11}e^{\beta x_2}, \quad E_{22}(x_2) = E^0_{22}e^{\beta x_2}, \quad G_{12}(x_2) = G^0_{12}e^{\beta x_2},$

dimensionless non-homogeneity parameter: $\beta a = (0.0\text{–}2.0)$,

$\delta^4 = E_{11}/E_{22} = (0.25, 0.5, 1.0, 3.0, 10.0)$,

$\kappa_0 = (-0.25, 0.0, 0.5, 1.0, 2.0, 5.0), \quad \nu = 0.15, 0.30, 0.45,$

generalized plane stress, 2×2 Gauss quadrature.

Notice that the average Young's modulus indicated above can be rewritten as $E = E^0e^{(\beta a)(x_2/a)}$, and thus the non-homogeneity parameter β enters the analysis through the dimensionless constant βa. Therefore $1/\beta$ is the length scale of non-homogeneity. This problem (i.e. crack perpendicular to material gradation) will be investigated for two different boundary conditions (BCs) (see Fig. 12(a) and (b)) and two loading cases. For the first set of BCs (Fig. 12(a)), $\beta a = (0.0\text{–}2.0)$ and for the second set of BCs (Fig. 12(b)), $\beta a = (0.0\text{–}1.0)$.

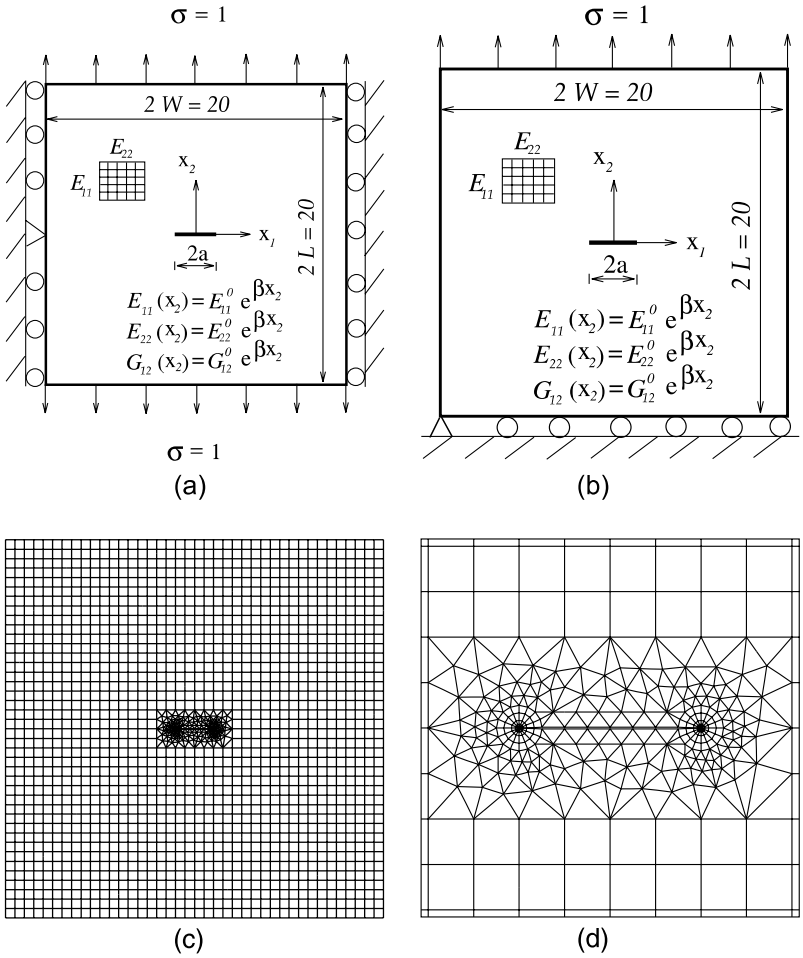

Fig. 12. Plate with a center crack perpendicular to the material gradation: (a) first set of BCs; (b) second set of BCs; (c) complete finite element mesh; (d) mesh detail using 4 rings (R4) and 16 sectors (S16) around crack tips.

6.3.1. Remote tension loading

Fig. 12(a) and (b) show a crack of length $2a$ located in a finite two-dimensional plate under remote uniform tension loading for two different boundary conditions. The complete mesh used in both cases is shown in Fig. 12(c), which is the same as that used for the example for a plate with a crack parallel to the material gradation (see Section 6.2 and Fig. 10(b)). Fig. 12(d) shows a detail with 4 rings (R4) and 16 sectors (S16) around the crack tips. The boundary conditions are prescribed such that, for Fig. 12(a), $u_1 = 0$ along the left and right edges and, in addition, $u_2 = 0$ for the node in the middle of the left edge, while for Fig. 12(b), $u_2 = 0$ along the bottom edge and in addition, $u_1 = 0$ at the left corner node of the bottom edge. The mesh has 1666 Q8, 303 T6, and 32 T6qp singular elements with a total of 2001 elements and 5851 nodes. The applied load corresponds to $\sigma_{22}(x_1, \pm 10) = \pm\sigma = \pm 1.0$ for the BCs in Fig. 12(a) and $\sigma_{22}(x_1, 10) = \sigma = 1.0$ for the BCs in Fig. 12(b).

Some representative results for the strain energy release rate, calculated from Eq. (25), for a non-homogeneous orthotropic plate under uniform tension considering two different BCs (cf. Fig. 12(a) and (b)) are plotted in Figs. 13–19. Notice in these figures that the normalized strain energy release rate $\mathscr{G}_0 = \pi\sigma^2 a/E^0$ corresponds to a homogeneous isotropic medium ($\beta a = 0$, $\kappa_0 = 1$, $\delta^4 = 1$).

Fig. 13 compares the FEM results for two different BCs and a fixed stiffness ratio $\delta^4 = 10$ with varying material non-homogeneity βa and shear parameter κ_0. Notice that the BCs and the Poisson's ratio (ν_{12}) (see Fig. 12(a) and (b)) have much influence on the strain energy release rates and, consequently, SIFs. The BCs of Fig. 12(a) prohibits the Poisson's effect of contraction in the x_1 direction. For these BCs (see Fig. 12(a)), the FEM results agree with the strain energy release rate ($\mathscr{G}$) obtained by Ozturk and Erdogan [23], which is a monotonically increasing function of κ_0 and βa. However, for the other BCs (see Fig. 12(b)), the results (dashed lines in Fig. 13) differ significantly from the previous ones (solid lines in Fig. 13). Notice that, for the case illustrated by Fig. 12(b), although $\mathscr{G}$ is still an increasing function of κ_0, it is a decreasing function of βa.

Figs. 14 and 15 show plots of the FEM results with varying βa and δ^4 for a fixed $\kappa_0 = 1$ considering the two BCs of Fig. 12(a) and (b), respectively. For the BCs of Fig. 12(a), Fig. 14 shows that $\mathscr{G}$ is an increasing function of δ^4 for $0 \leqslant \beta a \leqslant \approx 1.5$ and loses such behavior for $\beta a \geqslant \approx 1.5$, which agrees well with the results by Ozturk and Erdogan [23]. Moreover, $\mathscr{G}$ is a monotonically increasing function of βa. However, for the

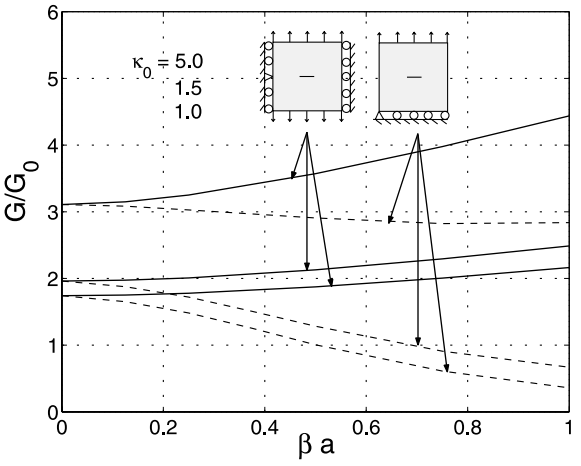

Fig. 13. Normalized strain energy release rate versus the non-homogeneity parameter βa and the shear parameter κ_0 considering uniformly applied tension ($\sigma_{22}(x_1, \pm L) = \pm\sigma$ for the left side BC and $\sigma_{22}(x_1, L) = \sigma$ for the right side BC) and $\delta^4 = E_{11}/E_{22} = 10.0$, $\nu = 0.3$, $\mathscr{G}_0 = \pi\sigma^2 a/E^0$. The solid lines correspond to the first set of BCs (see Fig. 12(a)) and the dashed lines correspond to the second set of BCs (see Fig. 12(b)).

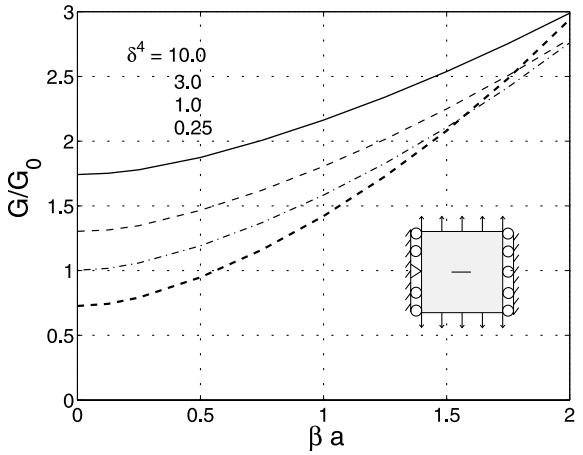

Fig. 14. Normalized strain energy release rate versus the non-homogeneity parameter βa and the stiffness parameter δ^4 considering uniformly applied tension with BCs of Fig. 12(a) and $\sigma_{22}(x_1, \pm L) = \pm\sigma$, $\kappa_0 = 1$, $\nu = 0.3$, $\mathcal{G}_0 = \pi\sigma^2 a/E^0$.

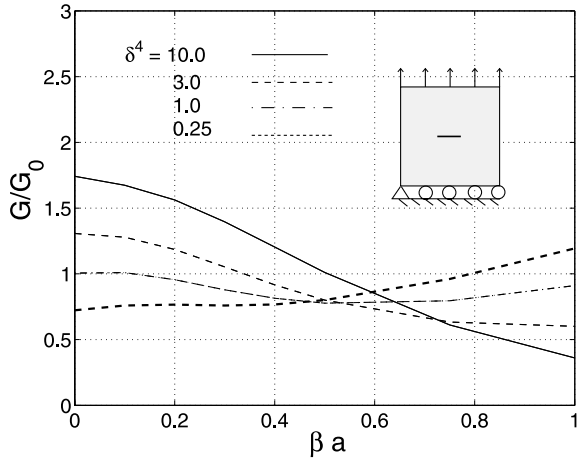

Fig. 15. Normalized strain energy release rate versus the non-homogeneity parameter βa and the stiffness parameter δ^4 considering uniformly applied tension with BCs of Fig. 12(b) and $\sigma_{22}(x_1, L) = \sigma$, $\kappa_0 = 1$, $\nu = 0.3$, $\mathcal{G}_0 = \pi\sigma^2 a/E^0$.

BCs of Fig. 12(b), the overall behavior is quite different as shown by Fig. 15, which indicates a change in the overall trends for $\beta a \approx 0.5$. The energy release rate $\mathcal{G}$ increases with δ^4 to the left of this point and it decreases to the right of this point. Note that $\mathcal{G}$ is a monotonically increasing function of βa for $\delta^4 = 0.25$ and a monotonically decreasing function of βa for $\delta^4 = 10$.

Figs. 16 and 17 show the FEM results with varying βa and δ^4 for the two BCs of Fig. 12(a) and (b), respectively. For the BCs of Fig. 12(a), Fig. 16 shows that $\mathcal{G}$ is an increasing function of βa, which matches well with the results by Ozturk and Erdogan [23], while for the BCs of Fig. 12(b), $\mathcal{G}$ loses such trends for βa as illustrated by Fig. 17.

Figs. 18 and 19 show the variation of $\mathcal{G}$ with βa and κ_0 for fixed $\delta^4 = 9$ considering the two BCs of Fig. 12(a) and (b), respectively. For the BCs of Fig. 12(a), Fig. 18 shows that $\mathcal{G}$ is an increasing function of βa and κ_0, which agrees with the results by Ozturk and Erdogan [23]. However, for the BCs of Fig. 12(b),

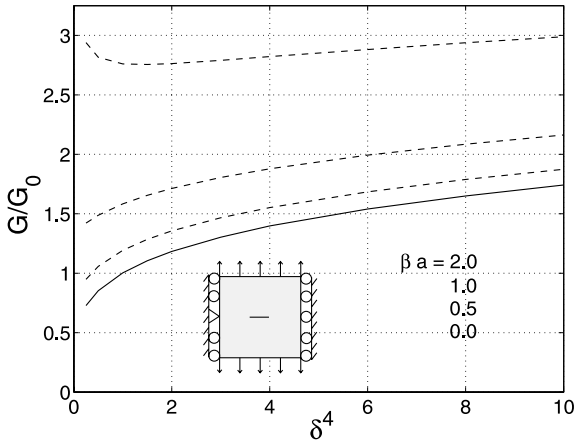

Fig. 16. Normalized strain energy release rate versus the stiffness parameter $\delta^4 = E_{11}/E_{22}$ and the non-homogeneity parameter βa considering uniformly applied tension with BCs of Fig. 12(a) and $\sigma_{22}(x_1, \pm L) = \pm\sigma$, $\kappa_0 = 1$, $\nu = 0.3$, $\mathscr{G}_0 = \pi\sigma^2 a/E^0$.

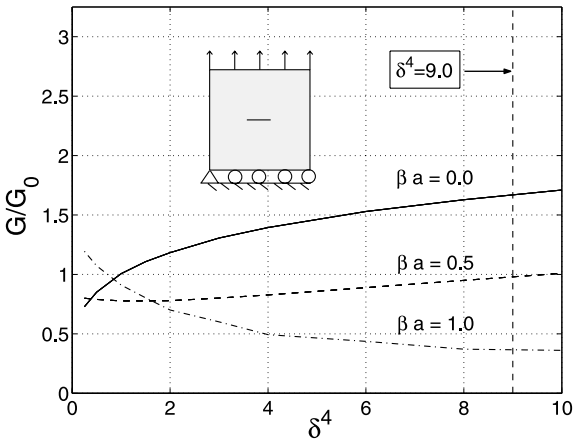

Fig. 17. Normalized strain energy release rate versus the stiffness parameter $\delta^4 = E_{11}/E_{22}$ and the non-homogeneity parameter βa considering uniformly applied tension with BCs of Fig. 12(b) and $\sigma_{22}(x_1, L) = \sigma$, $\kappa_0 = 1$, $\nu = 0.3$, $\mathscr{G}_0 = \pi\sigma^2 a/E^0$.

Fig. 19 shows that $\mathscr{G}$ is a decreasing function of βa and increasing function of κ_0. Moreover, consider the vertical line $\kappa_0 = 1$ in Fig. 19, and note that for increasing $\mathscr{G}$, the values of βa are $(1.0, 0.5, 0.0)$. This is consistent with the results of Fig. 17 (see vertical line in the graph).

6.3.2. Crack face loading

Fig. 20(a) shows a crack of length $2a$ located in a finite two-dimensional plate under either uniform crack face pressure (normal) loading or crack face shear loading. For uniform crack face pressure loading, the applied load corresponds to

$$\sigma_{22}(-1 \leqslant x_1 \leqslant 1, \pm 0) = \pm\sigma = \pm 1.0,$$

and for uniform crack face shear loading, the applied load corresponds to

$$\sigma_{12}(-1 \leqslant x_1 \leqslant 1, \pm 0) = \pm\tau = \pm 1.0.$$

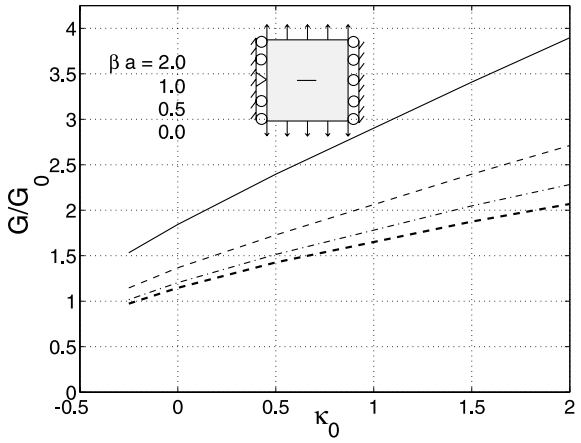

Fig. 18. Normalized strain energy release rate versus the shear parameter κ_0 and the non-homogeneity parameter βa considering uniformly applied tension with BCs of Fig. 12(a) and $\sigma_{22}(x_1, \pm L) = \pm\sigma$, $\delta^4 = 9$, $v = 0.3$, $\mathscr{G}_0 = \pi\sigma^2 a/E^0$.

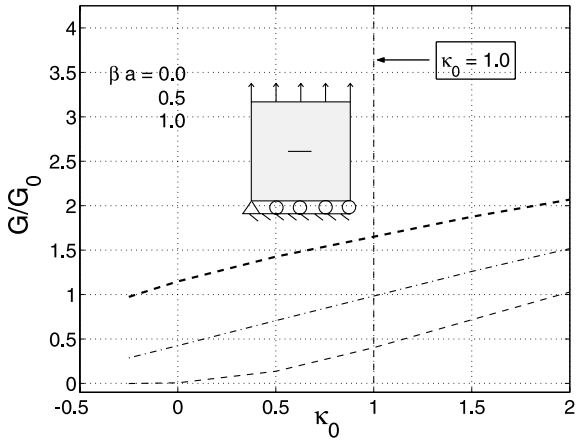

Fig. 19. Normalized strain energy release rate versus the shear parameter κ_0 and the non-homogeneity parameter βa considering uniformly applied tension with BCs of Fig. 12(b) and $\sigma_{22}(x_1, L) = \sigma$, $\delta^4 = 9$, $v = 0.3$, $\mathscr{G}_0 = \pi\sigma^2 a/E^0$.

The displacement boundary condition is prescribed such that $u_1 = u_2 = 0$ for the node in the middle of the left edge, and $u_2 = 0$ for the node in the middle of right edge. To address the influence of the crack tip discretization, two mesh configurations are used: one has 5 rings and 8 sectors (S8) around the crack tips (Fig. 20(b)) and the other has 4 rings (R4) and 16 sectors (S16) around the crack tips (Fig. 20(c)). The latter configuration is the same as those shown in Figs. 10(c) and 12(d). The results for this example are summarized in Figs. 21–25 and Tables 3–6.

Fig. 21 shows the increase in $K_I(a)$ with increasing βa and κ_0 under crack face pressure loading, which agrees with the results by Ozturk and Erdogan [23]. The influence of mesh discretization on fracture behavior is shown in Figs. 22 and 23, which illustrate the variation of SIFs with the non-homogeneity parameter βa and the shear parameter κ_0 under uniform crack face loading. Fig. 22 refers to the discretization with 8 sectors (S8) and Fig. 23 refers to the discretization with 16 sectors (S16) around the crack tips. Comparing Figs. 22 and 23, one notices that the results for $\kappa_0 = 1.0$, 1.5 and 5.0 are similar in both figures,

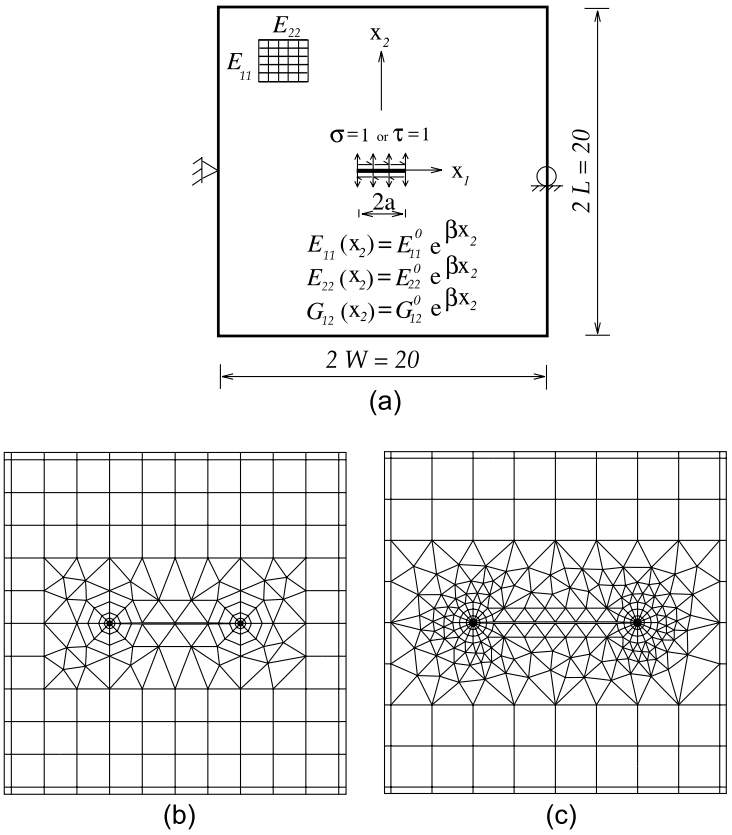

Fig. 20. Plate with a center crack perpendicular to the material gradation: (a) geometry and BCs; (b) mesh detail using 5 rings (R5) and 8 sectors (S8) around crack tips; (c) mesh detail using 4 rings (R4) and 16 sectors (S16) around crack tips.

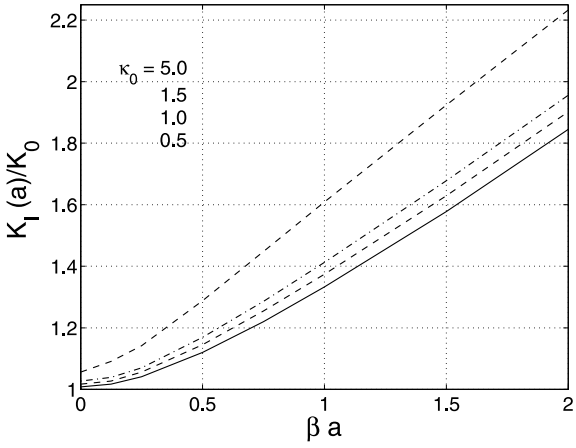

Fig. 21. Normalized strain energy release rate versus the non-homogeneity parameter βa and the shear parameter κ_0 under uniform crack face pressure loading, $\sigma_{22}(-a \leqslant x_1 \leqslant a, \pm 0) = \pm\sigma$, $\delta^4 = 0.25$, $\nu = 0.3$, $K_0 = \sigma\sqrt{\pi a}$.

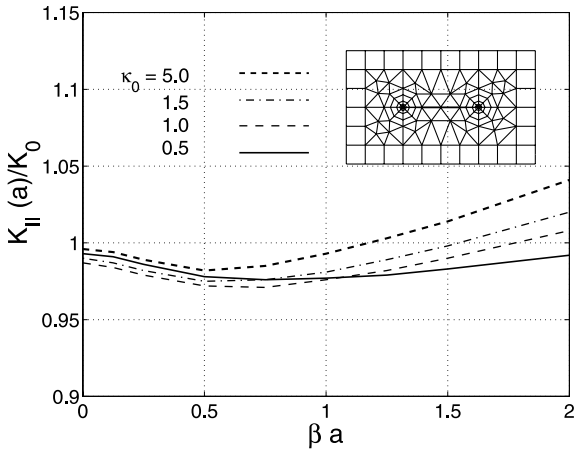

Fig. 22. Variation of the normalized SIFs versus the non-homogeneity parameter βa and the shear parameter κ_0 under uniform crack face shear loading, $\sigma_{12}(-a \leqslant x_1 \leqslant a, \pm 0) = \pm\tau$, $\delta^4 = 0.25$, $\nu = 0.3$, $K_0 = \tau\sqrt{\pi a}$ using 8 sectors (S8) around the crack tip.

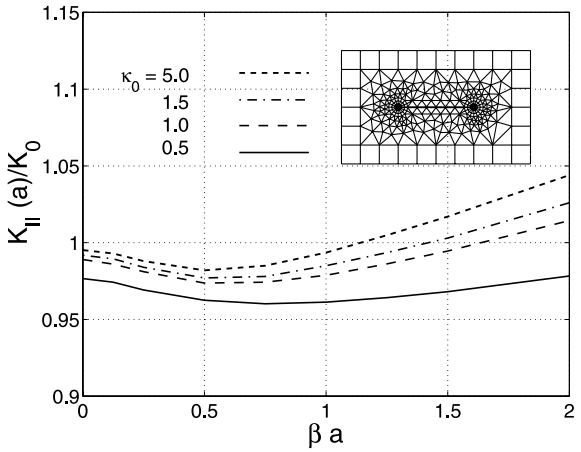

Fig. 23. Variation of the normalized SIFs versus the non-homogeneity parameter βa and the shear parameter κ_0 under uniform crack face shear loading, $\sigma_{12}(-a \leqslant x_1 \leqslant a, \pm 0) = \pm\tau$, $\delta^4 = 0.25$, $\nu = 0.3$, $K_0 = \tau\sqrt{\pi a}$ using 16 sectors (S16) around the crack tip.

but not the results for $\kappa_0 = 0.5$. In fact, the results in Fig. 23 (finer discretization: S16) are more reliable than those in Fig. 22 (coarser discretization: S8) and also agree with the results by Ozturk and Erdogan [23]. It is observed in Figs. 21–23 that K_{I} and K_{II} approach $K_0 = \sigma\sqrt{\pi a}$ and $K_0 = \tau\sqrt{\pi a}$, respectively, as βa tends to zero, while exact solutions are obtained by Ozturk and Erdogan [23]. This is due to numerical errors in the FEM which are absent in the integral equation method. However this type of method (i.e. based on integral equations) is much less general than the FEM. Fig. 24 shows a comparison of CODs by the FEM with those by Ozturk and Erdogan [23] for $\nu = 0.3$, $\kappa_0 = 0.5$, and $\delta^4 = 10$. Both results agree quite well. Fig. 25 shows the CSDs obtained by the FEM. It is interesting to observe that CSDs by the FEM are almost two times those by Ozturk and Erdogan [23]. The excellent agreement of the CODs and the factor of 2 for the CSDs seem to suggest a typo in the CSD results of reference [23]. The crack profiles in Fig. 25 are significantly influenced by the mesh discretization. A finer discretization along the crack surfaces (away from the tips) leads to a smoother profile (cf. Fig. 20(c)).

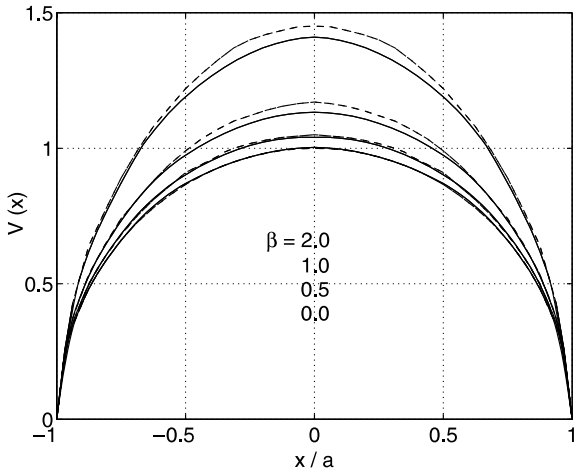

Fig. 24. Influence of the non-homogeneity parameter βa on the COD considering uniform crack face pressure loading, $\sigma_{22}(-a \leqslant x_1 \leqslant a, \pm 0) = \pm\sigma,\ \delta^4 = 10.0,\ \nu = 0.3,\ \kappa_0 = 0.5,\ V = (u_2(x_1, +0) - u_2(x_1, -0))/v_0,\ v_0 = a\sigma/E_2,\ (E_2 = E^0\delta/(2\sqrt{2}(\delta^2 + (E_{11}/2G_{12} - \nu_{12}))^{1/2}))$. The dotted lines represent the Ozturk and Erdogan's [23] analytical results and the solid lines show the FEM results.

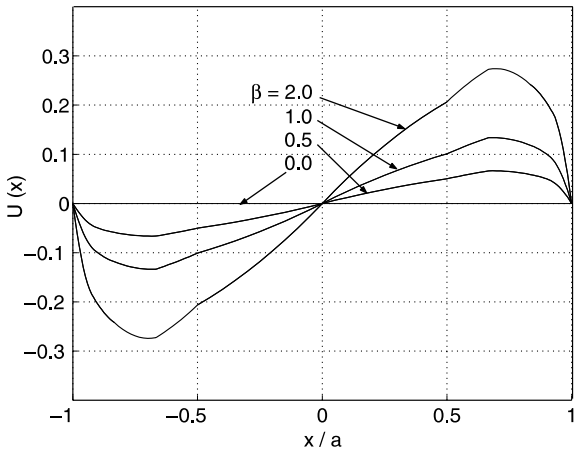

Fig. 25. Influence of the non-homogeneity parameter βa on the CSD considering uniform crack face pressure loading, $\sigma_{22}(-a \leqslant x_1 \leqslant a, \pm 0) = \pm\sigma,\ \delta^4 = 10.0,\ \nu = 0.3,\ \kappa_0 = 0.5,\ U = (u_1(x_1, +0) - u_1(x_1, -0))/u_0,\ u_0 = a\sigma/E_1,\ (E_1 = E^0\delta^2/(2\sqrt{2}(\delta^2 + (E_{11}/2G_{12} - \nu_{12}))^{1/2}))$.

Several SIF results are presented in Tables 3–6 and are also compared with the results obtained by Ozturk and Erdogan [23]. Table 3 shows the effect of loading conditions and the non-homogeneity parameter βa on the normalized SIFs for uniform crack face pressure loading and for uniform crack face shear loading using both the MCC and DCT. Tables 4 and 5 show the effect of the Poisson's ratio on the normalized SIFs in a non-homogeneous orthotropic plate with the uniform crack face pressure loading and shear loading, respectively. To show the influence of mesh discretization on the SIFs, Table 6 presents mixed-mode SIFs in a non-homogeneous orthotropic plate with crack face pressure loading considering $\beta = 0.5$, $\kappa_0 = 5.0$, and $\delta^4 = 10$. Notice that the mesh with 16 sectors (S16) leads to results that are closer to

Table 3
The effect of the loading conditions on the normalized SIFs in a non-homogeneous orthotropic plate for the mixed-mode problem considering $\kappa_0 = 0.5$ ($K_0 = \sigma\sqrt{\pi a}$ for uniform crack face pressure loading and $K_0 = \tau\sqrt{\pi a}$ for uniform crack face shear loading)

Method	βa	σ		τ	
		$K_I(a)/K_0$	$K_{II}(a)/K_0$	$K_I(a)/K_0$	$K_{II}(a)/K_0$
Ozturk and Erdogan [23]	0.0	1.0	0.0	0.0	1.0
	0.1	1.0115	0.0250	−0.0494	0.9989
	0.25	1.0489	0.0627	−0.1191	0.9968
	0.50	1.1351	0.1263	−0.2217	0.9965
	1.0	1.3494	0.2587	−0.3682	1.0071
	2.0	1.8580	0.5529	−0.5725	1.0499
MCC S16, $\Delta a = a/24$	0.0	1.021	0.0	0.0	0.992
	0.1	1.0273	0.0246	−0.0484	0.9907
	0.25	1.0550	0.0601	−0.1150	0.9850
	0.50	1.1351	0.1204	−0.2126	0.9788
	1.0	1.3495	0.2458	−0.3685	0.9884
	2.0	1.8663	0.5226	−0.5940	1.0350
DCT S16, $\Delta a = a/24$	0.0	1.0302	0.0	0.0	0.9811
	0.1	1.0352	0.0242	−0.0492	0.9799
	0.25	1.0618	0.0609	−0.1196	0.9749
	0.50	1.1390	0.1227	−0.2219	0.9687
	1.0	1.3444	0.2515	−0.3857	0.9777
	2.0	1.8240	0.5377	−0.6245	1.0189

Table 4
The effect of the Poisson's ratio on the normalized SIFs in a non-homogeneous orthotropic plate with crack face (normal) pressure loading for the mixed-mode problem ($\kappa_0 = 5.0,\ K_0 = \sigma\sqrt{\pi a}$)

Method	βa	δ^4	0.25			10.0		
		ν	0.15	0.30	0.45	0.15	0.30	0.45
Ozturk and Erdogan [23]	0.5	$K_I(a)/K_0$	1.2516	1.2596	1.2674	1.0748	1.0776	1.0804
		$K_{II}(a)/K_0$	0.1259	0.1259	0.1259	0.1252	0.1252	0.1251
	1.0	$K_I(a)/K_0$	1.5589	1.5739	1.5884	1.1892	1.1955	1.2017
		$K_{II}(a)/K_0$	0.2555	0.2557	0.2558	0.2511	0.2512	0.2512
MCC S16, $\Delta a = a/24$	0.5	$K_I(a)/K_0$	1.2536	1.2615	1.2694	1.073	1.076	1.079
		$K_{II}(a)/K_0$	0.1196	0.1196	0.1196	0.1297	0.1297	0.1298
	1.0	$K_I(a)/K_0$	1.5611	1.5763	1.5910	1.1881	1.1949	1.2011
		$K_{II}(a)/K_0$	0.2402	0.2403	0.2404	0.2415	0.2415	0.2414
DCT S16, $\Delta a = a/24$	0.5	$K_I(a)/K_0$	1.267	1.275	1.282	1.082	1.084	1.086
		$K_{II}(a)/K_0$	0.1166	0.1167	0.1169	0.1143	0.1144	0.1144
	1.0	$K_I(a)/K_0$	1.563	1.578	1.591	1.1960	1.1994	1.2051
		$K_{II}(a)/K_0$	0.2363	0.2366	0.2370	0.2273	0.2274	0.2274

those by Ozturk and Erdogan [23] than the mesh with 8 sectors (S8), which confirms the need for careful crack tip mesh discretization in order to obtain satisfactory SIF results by the FEM. In summary, for this example, the MCC and DCT give accurate SIF results in comparison with those by Ozturk and Erdogan [23].

Table 5
The effect of the Poisson's ratio on the normalized SIFs in a non-homogeneous orthotropic plate with crack face shear loading for the mixed-mode problem ($\kappa_0 = 5.0,\ K_0 = \tau\sqrt{\pi a}$)

Method	βa	δ^4	0.25			10.0		
		v	0.15	0.3	0.45	0.15	0.3	0.45
Ozturk and Erdogan [23]	0.5	$K_I(a)/K_0$	−0.1980	−0.1971	−0.1963	−0.0366	−0.0365	−0.0365
		$K_{II}(a)/K_0$	0.9898	0.9915	0.9931	0.9956	0.9961	0.9965
	1.0	$K_I(a)/K_0$	−0.3203	−0.3186	−0.3169	−0.0660	−0.0657	−0.0654
		$K_{II}(a)/K_0$	0.9888	0.9921	0.9953	0.9913	0.9925	0.9938
MCC S16, $\Delta a = a/24$	0.5	$K_I(a)/K_0$	−0.1883	−0.1872	−0.1861	−0.0340	−0.0341	−0.0339
		$K_{II}(a)/K_0$	0.9529	0.9546	0.9359	0.9168	0.9173	0.9179
	1.0	$K_I(a)/K_0$	−0.3034	−0.3012	−0.2991	−0.0598	−0.0595	−0.0591
		$K_{II}(a)/K_0$	0.9495	0.9529	0.9557	0.9117	0.9134	0.9145
DCT S16, $\Delta a = a/24$	0.5	$K_I(a)/K_0$	−0.2009	−0.1997	−0.1987	−0.0349	−0.0344	−0.0343
		$K_{II}(a)/K_0$	0.9224	0.9241	0.9252	0.8507	0.8519	0.8919
	1.0	$K_I(a)/K_0$	−0.3264	−0.3242	−0.3221	−0.0638	−0.0620	−0.0615
		$K_{II}(a)/K_0$	0.9185	0.9213	0.9241	0.8445	0.8479	0.8496

Table 6
Effect of crack tip mesh discretization on the SIFs in a non-homogeneous orthotropic plate with crack face pressure loading for the mixed-mode problem considering $v = (0.15, 0.30, 0.45)$ and $\beta a = 0.5$, $\kappa_0 = 5.0$, $\delta^4 = 10$, $K_0 = \sigma\sqrt{\pi a}$

Method	v	0.15	0.30	0.45
Ozturk and Erdogan [23]	$K_I(a)/K_0$	1.0748	1.0776	1.0804
	$K_{II}(a)/K_0$	0.1252	0.1252	0.1251
MCC S8, $\Delta a = a/32$	$K_I(a)/K_0$	1.070	1.074	1.076
	$K_{II}(a)/K_0$	0.1639	0.1646	0.1653
MCC S16, $\Delta a = a/24$	$K_I(a)/K_0$	1.073	1.076	1.079
	$K_{II}(a)/K_0$	0.1297	0.1297	0.1298

6.4. Two interacting offset cracks

This example is based on the experiments for SIFs for interacting cracks conducted by Mehdi-Soozani et al. [39]. They have used polycarbonate PSM1 (Product of Measurements Group, Inc.), which is a photoelastic material free of time-edge effects and exhibits very little creep at room temperature. The configuration that they [39] tested and analyzed is illustrated by Fig. 26(a), which shows two interacting offset cracks of length $2a$ located with angles $\theta = 0°$ and $\theta = 45°$ in a finite two-dimensional plate under uniform remote tension. Fig. 26(b) shows the complete finite element mesh configuration, and Fig. 26(c) shows the mesh detail with 16 sectors (S16) around the four crack tips. The applied load corresponds to $\sigma_{22} = \pm\sigma = \pm 1.22$ MPa along the top and bottom edges. The displacement boundary condition is prescribed such that $u_1 = u_2 = 0$ for the node in the middle of the left edge and $u_2 = 0$ for the node in the middle of the right edge. For the isotropic case, we consider the plate as homogeneous. For the orthotropic case, the variations of $E_{11}(\boldsymbol{x})$, $E_{22}(\boldsymbol{x})$, and $G_{12}(\boldsymbol{x})$ are assumed to be exponential and non-proportional functions, while the Poisson's ratio is constant. The mesh has 2621 Q8, 574 T6, and 64 T6qp elements with a total of 3259 elements and 9460 nodes. The following data were used for the FEM analysis:

$L = 381$ mm, $W = 114.3$ mm, $t = 3.17$ mm, $2a = 20.32$ mm
For isotropic homogeneous case:
$E = 2390$ MPa, $v = 0.38$,

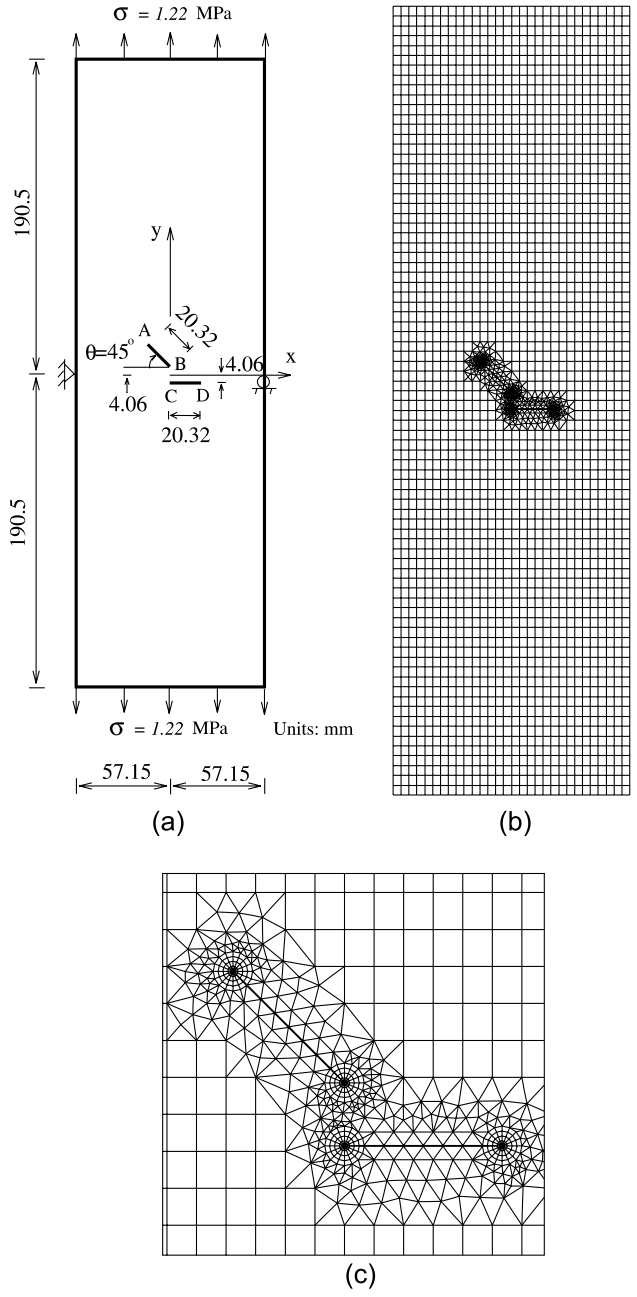

Fig. 26. Two interacting offset cracks in a finite plate; (a) geometry and BCs; (b) complete finite element mesh; (c) mesh detail showing 6 rings (R6) and 16 sectors (S16) around crack tips. (Units: N, mm).

For orthotropic FGM case:

$E_{11}(x_1) = E_{11}^0 e^{\alpha x_1}, \quad E_{22}(x_1) = E_{22}^0 e^{\beta x_1}, \quad G_{12}(x_1) = G_{12}^0 e^{\gamma x_1},$

$E_{11}^0 = 2390 \text{ MPa}, \quad E_{22}^0 = 1195 \text{ MPa}, \quad G_{12}^0 = 688.7 \text{ MPa}, \quad \nu_{12} = 0.38,$

$(\alpha, \beta, \gamma) = (0.01970, 0.01576, 0.01183), \quad$ generalized plane stress, $\quad 2 \times 2$ Gauss quadrature.

Table 7
The normalized SIFs with two interacting offset cracks for uniform remote tension loading considering a homogeneous isotropic material and also an orthotropic FGM with $(\alpha, \beta, \gamma) = (0.01970, 0.01576, 0.01183)$. The normalizing factor is $K_0 = \sigma\sqrt{\pi a}$

Problem	Method	SIFs	TIP A	TIP B	TIP C	TIP D
Isotropic homogeneous	Mehdi-Soozani et al. [39]	$\mathbf{K_I/K_0}$ **(exper.)**	**0.64**	**0.70**	**1.14**	**1.16**
		$\mathbf{K_{II}/K_0}$ **(exper.)**	**−0.59**	**−0.58**	**0.14**	**0.04**
		K_I/K_0 (numer.)	0.79	0.64	1.18	1.18
		K_{II}/K_0 (numer.)	−0.65	−0.61	0.14	0.01
	MCC	K_I/K_0	0.613	0.752	1.129	1.124
		K_{II}/K_0	−0.576	−0.614	0.130	0.012
	DCT	K_I/K_0	0.616	0.756	1.131	1.129
		K_{II}/K_0	−0.565	−0.602	0.128	0.005
Orthotropic FGM (proposed)	MCC	K_I/K_0	0.631	0.872	1.216	1.341
		K_{II}/K_0	−0.607	−0.630	0.155	0.021
	DCT	K_I/K_0	0.633	0.875	1.220	1.343
		K_{II}/K_0	−0.594	−0.613	0.152	0.004

Table 7 shows FEM results for SIFs using the MCC and DCT for the isotropic homogeneous case in comparison with experimental results and numerical results using the boundary element method (BEM) by Mehdi-Soozani et al. [39]. The present results for the isotropic homogeneous case show good agreement with the experimental and BEM results. Notice that the MCC results are closer to the experimental results than the BEM. Table 7 also shows FEM results for SIFs in orthotropic FGM with non-proportional material gradation using the MCC and DCT for which there are no available reference solutions.

7. Conclusions and extensions

FGMs feature an intentional material property grading, whereas the property orientation or orthotropy is usually a result of material processing/manufacturing. Due to the need to understand the mechanics of such materials, this paper presents a general purpose finite element formulation and implementation for elasticity and mixed-mode fracture analysis of orthotropic FGMs where cracks are arbitrarily oriented with respect to the principal axes of orthotropy. The DCT and the MCC method are assessed by using carefully designed singular and transition elements around the crack tips in orthotropic FGMs. From extensive numerical results presented, the following conclusions are made. The MCC and DCT provide very accurate SIFs for mixed-mode crack problems in orthotropic FGMs with cracks either aligned with the principal directions of orthotropy or arbitrarily oriented. Moreover, in contrast to homogeneous materials, Poisson's ratio and boundary conditions are found to have significant influence on the energy release rates and, consequently, SIFs in mixed-mode crack problems in orthotropic FGMs. Thus, special attention is required in defining Poisson's ratio and boundary conditions for problems involving such materials.

Acknowledgements

We gratefully acknowledge the support from the National Science Foundation (NSF) under grant no. CMS-0115954 (Mechanics and Materials Program) and from the NASA Ames Research Center (NAG 2-1424) to the University of Illinois at Urbana-Champaign. At NASA, Dr. Tina Panontin serves as the project Technical Monitor. We thank Mr. M.C. Walters for useful suggestions.

References

[1] Hirai T. Functionally gradient materials and nanocomposites. In: Holt JB, Koizumi M, Hirai T, Munir ZA, editors. Proceedings of the Second International Symposium on Functionally Gradient Materials, Ceramic Transactions, vol 34. Westerville, Ohio: The American Ceramic Society; 1993. p. 11–20.

[2] Delale F, Erdogan F. The crack problem for a nonhomogeneous plane. J Appl Mech 1983;50:609–14.

[3] Erdogan F, Wu BH. In: Analysis of FGM specimen for fracture toughness testing. Ceramic Transactions, vol 34. Westerville, Ohio: The American Ceramic Society; 1993. p. 39–46.

[4] Marur PR, Tippur HV. Numerical analysis of crack-tip fields in functionally graded materials with a crack normal to the elastic gradient. Int J Solids Struct 2000;37:5353–70.

[5] Noda N, Jin ZH. Thermal stress intensity factors for a crack in a strip of a functionally graded materials. Int J Solids Struct 1993;30:1039–56.

[6] Jin ZH, Noda N. An internal crack parallel to the boundary of a nonhomogeneous half plane under thermal loading. Int J Eng Sci 1993;31:793–806.

[7] Erdogan F, Wu BH. Crack problems in FGM layers under thermal stresses. J Therm Stresses 1996;19:237–65.

[8] Jin ZH, Batra RC. Stress intensity relaxation at the tip of an edge crack in a functionally graded material subjected to a thermal shock. J Therm Stresses 1996;19:317–39.

[9] Wang BL, Han JC, Du SY. Crack problems for functionally graded materials under transient thermal loading. J Therm Stresses 2000;23(2):143–68.

[10] Jin ZH, Paulino GH. Transient thermal stress analysis of an edge crack in a functionally graded material. Int J Fract 2001;107(1):73–98.

[11] Wang BL, Noda N. Thermally induced fracture of a smart functionally graded composite structure. Theor Appl Fract Mech 2001;35(2):93–109.

[12] Anlas G, Santare MH, Lambros J. Numerical calculation of stress intensity factors in functionally graded materials. Int J Fract 2000;104:131–43.

[13] Chen J, Wu L, Du S. A modified *J* integral for functionally graded materials. Mech Res Commun 2000;27(3):301–6.

[14] Eischen JW. Fracture of nonhomogeneous materials. Int J Fracture 1987;34:3–22.

[15] Kim JH, Paulino GH. Finite element evaluation of mixed mode stress intensity factors in functionally graded materials. Int J Numer Meth Eng 2002;53(8):1903–35.

[16] Gu P, Dao M, Asaro RJ. A simplified method for calculating the crack-tip field of functionally graded materials using the domain integral. ASME J Appl Mech 1999;66(1):101–8.

[17] Bao G, Wang L. Multiple cracking in functionally graded ceramic/metal coatings. Int J Solids Struct 1995;32(19):2853–71.

[18] Bao G, Cai H. Delamination cracking in functionally graded coating/metal substrate systems. Acta Mechanica 1997;45(3):1055–66.

[19] Sampath S, Herman H, Shimoda N, Saito T. Thermal spray processing of FGMs. MRS Bull 1995;20(1):27–31.

[20] Kaysser WA, Ilschner B. FGM research activities in Europe. MRS Bull 1995;20(1):22–6.

[21] Gu P, Asaro RJ. Cracks in functionally graded materials. Int J Solids Struct 1997;34(1):1–17.

[22] Ozturk M, Erdogan F. Mode I crack problem in an inhomogeneous orthotropic medium. Int J Eng Sci 1997;35(9):869–83.

[23] Ozturk M, Erdogan F. The mixed mode crack problem in an inhomogeneous orthotropic medium. Int J Fract 1999;98:243–61.

[24] Lekhnitskii SG. Anisotropic plates. New York: Gordon and Breach Science Publishers; 1968.

[25] Shih CF, de Lorenzi HG, German MD. Crack extension modeling with singular quadratic isoparametric elements. Int J Fract 1976;12:647–51.

[26] Irwin GR. Analysis of stresses and strains near the end of a crack traversing a plate. ASME J Appl Mech 1957;24:354–61.

[27] Rybicki EF, Kanninen MF. A finite element calculation of stress intensity factors by a modified crack closure integral. Eng Fract Mech 1977;9:931–8.

[28] Raju IS. Calculation of strain-energy release rates with high order and singular finite elements. Eng Fract Mech 1987;28(3):251–74.

[29] Sih GC, Paris PC, Irwin GR. On cracks in rectilinearly anisotropic bodies. Int J Fract Mech 1965;1:189–203.

[30] Ramamurthy TS, Krishmamurthy T, Narayana KB, Vijayakumar K, Dataguru B. Modified crack closure integral method with quarter point elements. Mech Res Commun 1986;13(4):179–86.

[31] Kim JH, Paulino GH. Isoparametric graded finite elements for nonhomogeneous isotropic and orthotropic materials. ASME J Appl Mech, in press.

[32] Paulino GH, Kim JH. The weak patch test for nonhomogeneous materials modeled with graded finite elements, submitted for publication.

[33] Wawrzynek PA. Interactive finite element analysis of fracture processes: an integrated approach, MS Thesis, Cornell University, 1987.

[34] Wawrzynek PA, Ingraffea AR. Discrete modeling of crack propagation: theoretical aspects and implementation issues in two and three dimensions. Report 91-5, School of Civil Engineering and Environmental Engineering, Cornell University, 1991.

[35] Kim JH, Paulino GH. Mixed-mode *J*-integral formulation and implementation using graded elements for fracture analysis of nonhomogeneous orthotropic materials, submitted for publication.
[36] Krenk S. On the elastic constants of plane orthotropic elasticity. J Compos Mat 1979;13:108–16.
[37] Atluri SN, Kobayashi AS, Nakagaki M. A finite element program for fracture mechanics analysis of composite material. Fract Mech Compos, ASTM STP 1975;593:86–98.
[38] Wang SS, Yau JF, Corten HT. A mixed mode crack analysis of rectilinear anisotropic solids using conservation laws of elasticity. Int J Fract 1980;16:247–59.
[39] Mehdi-Soozani A, Miskioglu I, Burger CP, Rudolphi TJ. Stress intensity factors for interacting cracks. Eng Fract Mech 1987;27:345–59.